

# Convective heat transfer on coolant hoses

Aghigh Merikhi

DEPARTMENT OF MECHANICS AND MARITIME SCIENCES



MASTER'S THESIS IN SUSTAINABLE ENERGY SYSTEMS

# Convective heat transfer on coolant hoses

AGHIGH MERIKHI

Department of Mechanics and Maritime Sciences  
Division of Vehicle Engineering and Autonomous Systems  
CHALMERS UNIVERSITY OF TECHNOLOGY  
Göteborg, Sweden 2024

Convective heat transfer on coolant hoses  
AGHIGH MERIKHI

© AGHIGH MERIKHI, 2024-06-10

Supervisor: Randi Franzke, Volvo Cars  
Examiner: Simone Sebben, Department of Mechanics and Maritime Sciences

Department of Mechanics and Maritime Sciences  
Division of Vehicle Engineering and Autonomous Systems  
Chalmers University of Technology  
SE-412 96 Göteborg  
Sweden  
Telephone: + 46 (0)31-772 1000

Cover:  
Image of air streamlines over coolant pipe in the experimental rig

Department of Mechanics and Maritime Sciences  
Göteborg, Sweden 2024-06-10

Convective heat transfer on coolant hoses  
Master's thesis in Master's Sustainable Energy Systems  
AGHIGH MERIKHI  
Department of Mechanics and Maritime Sciences  
Division of Vehicle Engineering and Autonomous Systems  
Chalmers University of Technology

## Abstract

This master thesis inspects the convective heat transfer on coolant hoses within electric vehicle (EV) under-hood parts. The focus is on the influence of air flow generated by a fan on the convective heat loss from the coolant hoses and its following impact on the overall cooling system performance. Due to the low magnitude of heat loss which cannot be recognized from measurement system errors in a complete vehicle test, a simplified experimental rig is used. Computational Fluid Dynamics (CFD) simulations are done to provide a comprehensive analysis comparable with experimental results. Key factors such as coolant flow rate and air temperature are studied for their impact on heat transfer coefficients. The study objects to improve the accuracy of one-dimensional simulation models by validating them by the experimental data achieved. The results indicate the noteworthy influence of coolant flow rate on the heat transfer coefficient and underline the significance of using highly accurate measurement devices, mainly flowmeters, to minimize uncertainty and error in experimental data. This research contributes to the optimization of EV cooling systems by offering a better understanding of the convective heat transfer mechanisms impacting coolant hoses.

Key words: convective heat transfer, coolant hoses, electric vehicles, CFD simulation, cooling system performance, heat transfer coefficient.



# Contents

Abstract .....	I
Contents .....	III
Preface.....	IX
Notations .....	X
1 Introduction.....	1
1.1 Background .....	1
1.1.1 Battery thermal management (BTM).....	2
1.1.2 Motor thermal management (MTM).....	2
1.1.3 Cabin thermal management (CTM).....	2
1.1.4 Integrated Thermal Management System .....	3
1.2 Previous studies.....	3
1.3 Objective .....	4
2 Theory .....	5
2.1 Heat transfer .....	5
2.1.1 Conduction .....	5
2.1.2 Convection .....	5
2.1.3 Heat transfer relations .....	6
2.1.4 Thermal resistance .....	6
2.1.5 Convective heat transfer coefficient .....	8
2.1.6 Energy balance.....	10
2.2 Fluid dynamics .....	11
2.2.1 Computational fluid dynamics.....	12
3 Methodology.....	15
3.1 Experiment .....	15
3.1.1 Geometry.....	15
3.1.2 Measurement.....	16
3.1.3 Measurement system setup .....	17
3.1.4 Study of experiment environment.....	19
3.1.5 Test cases .....	21
3.1.6 Additional improvements to the experiment.....	22
3.1.7 Repeatability .....	26
3.2 Computational fluid dynamics simulation .....	26
3.2.1 Study of geometry scale.....	26
3.2.2 Mesh for box model .....	28

3.2.3	Room model mesh .....	32
3.2.4	Models for steady and transient simulation .....	34
3.2.5	Room model mesh analysis .....	35
3.2.6	Comparison of box model and room model .....	39
3.2.7	Comparison of turbulence models on room model.....	42
4	Results and discussion .....	45
4.1	Comparison of coolant temperature difference .....	45
4.1.1	Impact of air velocity .....	46
4.1.2	Impact of coolant flow .....	48
4.1.3	Impact of coolant temperature .....	48
4.2	Comparison of heat transfer coefficient .....	49
4.3	Additional simulations .....	51
4.3.1	Upstream wall study .....	51
5	Conclusions.....	55
6	References.....	57

## List of figures

Figure 2.1 Series of thermal resistances between cross air flow and fluid in the pipe [13].....	8
Figure 2.2 Energy balance of in a pipe cross sectional control volume [13].....	10
Figure 3.1 Geometry specifications of the rig .....	15
Figure 3.2 Coolant circuit .....	16
Figure 3.3 Rig setup: Fan and box .....	18
Figure 3.4 Rig setup: Inlet .....	18
Figure 3.5 Rig setup: Outlet.....	19
Figure 3.6 Rig setup: Inside the box .....	19
Figure 3.7 Configuration of measurement devices .....	19
Figure 3.8 Schematic picture of the room where rig is located .....	20
Figure 3.9 (a) Air velocity in the upper hot wire probe and (b) thermocouples average temperature during test before environment study .....	20
Figure 3.10 comparison of standard deviation of air velocity and thermocouples average during test between room conditions cases .....	21
Figure 3.11 Coolant temperature difference comparison between experiment 1 and 2 .....	23
Figure 3.12 Comparison between turbine and magnetic flow meter measurement results in case 1 .....	23
Figure 3.13 Coolant temperature difference comparison between experiment 1 to 3.	24
Figure 3.14 Temperature results of case 1 from thermocouples in coolant pipe's inlet and outlet (a) before and (b) after correction .....	25
Figure 3.15 Coolant temperature difference comparison between experiment 1 to 4.	25
Figure 3.16 Repeatability test results in (a) coolant temperature difference comparison and (b) coolant temperature difference standard deviation between tests for each case .....	26
Figure 3.17 Geometry modelled in box model .....	27
Figure 3.18 Geometry modelled in room model.....	27
Figure 3.19 Contact between coolant, pipe and air regions in mesh for box model....	28
Figure 3.20 Mesh for box model.....	31
Figure 3.21 Mesh for room model .....	32

Figure 3.22 Rotating part of the mesh in different viewpoints .....	33
Figure 3.23 Left) fan geometry and right) fan geometry combined with fan rotating region .....	34
Figure 3.24 Room sizing of mesh 1 for room model.....	35
Figure 3.25 In picture a, b and c, temperature contours in the plane of the air temperature thermocouples for case 1 are shown for simulations with mesh 4, 5 and 6, respectively. The location of thermocouples are shown in temperature contours with black dots. d) Temperature contour drawn by the thermocouples' experimental data. ....	36
Figure 3.26 In picture a, b and c, air velocity contours in the plane of the hot wire probes for case 1 are shown for simulations with mesh 4, 5 and 6, respectively. The location of hot wire probes are shown in temperature contours with black dots. d) Comparison of air velocities in the hot wite probes with air velocities in the location of hot wire probes in simulations with mesh 4, 5 and 6. ....	37
Figure 3.27 Comparison of coolant inlet and outlet temperature difference between meshes for room model.....	38
Figure 3.28 Air velocity vector contour in the room model with mesh 5 for case 1 ...	38
Figure 3.29 Comparison of box and room model .....	39
Figure 3.30 a, b, c, d)Air velocity contours for simulations with box 1, box 2, box 3 and room models, respectively. ....	40
Figure 3.31 a, b, c, d) heat transfer on pipe surface in box 1, box 2, box 3 and room models, respectively.....	41
Figure 3.32 Model study on Case 1 .....	42
Figure 3.33 a, b, c) Air velocity contour for steady simulation with k-epsilon model, steady simulation with k-omega model and transient simulation with DES model, respectively .....	43
Figure 3.34 a, b, c) heat transfer on pipe surface in steady simulation with k-epsilon model, steady simulation with k-omega model and transient simulation with DES model, respectively .....	44
Figure 4.1 Comparison of coolant temperature difference in experiment and simulation. Form Case 1 to 5, the coolant volumetric flow is 0.05 l/s and from Case 6 to 9, the coolant volumetric flow is 0.01 l/s.....	45
Figure 4.2 Effect of air velocityon coolant temperature difference in coolant volumetric flow of 0.05 l/s.....	46

Figure 4.3 Effect of air velocity on coolant temperature difference in 55 °C temperature difference between coolant inlet and air .....	47
Figure 4.4 Effect of coolant volumetric flow on coolant temperature difference in fan rotation rate of 1500 rpm .....	48
Figure 4.5 Effect of temperature difference between coolant pipe outlet and air with fan rotation of 1500 rpm .....	48
Figure 4.6 Comparison of overall heat transfer coefficient in experiment and simulation. From Case 1 to 5, the coolant volumetric flow is 0.05 l/s and from Case 6 to 9, the coolant volumetric flow is 0.01 l/s.....	49
Figure 4.7 Effect of air velocity on overall heat transfer coefficient in 55 °C temperature difference between coolant inlet and air .....	50
Figure 4.8 Effect of coolant volumetric flow on overall heat transfer coefficient in fan rotation rate of 1500 rpm .....	50
Figure 4.9 Geometry of wall added upstream of the pipe in mesh for room.....	52
Figure 4.10 a) Comparison of coolant temperature difference between simulations of main cases and cases with upstream wall b) Comparison of overall heat transfer coefficient between simulations of main cases and cases with upstream wall.....	52
Figure 4.11 a) Comparison of effect of coolant volumetric flow on heat transfer coefficient between simulation results with and without upstream wall b) Comparison of effect of fan rotation rate on heat transfer coefficient between simulation results with and without upstream wall.....	53
Figure 4.12 a, b) Air velocity contours from case 1 simulation without and with upstream wall, respectively.....	53
Figure 4.13 a, b) Heat transfer coefficient on pipe surface without and with upstream wall.....	54

## List of tables

Table 2.1 Coefficients for equation (2.17) [13] .....	9
Table 3.1 Test cases' setting properties.....	22
Table 3.2 Mesh study for box model .....	30
Table 3.3 Specifications of mesh for box model .....	30
Table 3.4 Coolant domain comparison study .....	31
Table 3.5 Mesh study for room different boundary conditions .....	36
Table 3.6 Box models specifications .....	39

## **Preface**

The project was conducted at Volvo Cars Corporation as part of the Sustainable Energy Systems master's program at Chalmers University of Technology, with the invaluable support of my supervisor, Randi Franzke, and my examiner at Chalmers, Professor Simone Sebben.

I want to express my gratitude to everyone at Volvo Cars in the Thermal Efficiency group for their help and the resources they provided. My supervisor, Randi Franzke, has my sincere gratitude for making this thesis opportunity possible. Her unwavering patience, positivity, and support were invaluable during this project.

Additionally, I would like to express my sincere thanks to Emil Willeson for his invaluable advice and support throughout the experiments. I also want to express my gratitude to the Thermal Efficiency team for their helpful advice and cooperation. Finally, I would like to thank Professor Simone Sebben from Chalmers University of Technology for her supervision during my master's thesis and for being my examiner.

Göteborg March 2024-06-10

AGHIGH MERIKHI

# Notations

## Abbreviations

<i>AC</i>	Air Conditioning
<i>BEV</i>	Battery Electric Vehicle
<i>BTM</i>	Battery Thermal Management
<i>CFD</i>	Computational Fluid Dynamics
<i>COP</i>	Coefficient of Performance
<i>CTM</i>	Cabin Thermal Management
<i>DES</i>	Detached Eddy Simulation
<i>ED</i>	Electric Drive
<i>EM</i>	Electric Motor
<i>EV</i>	Electric Vehicle
<i>EVTM</i>	Electric Vehicle Thermal Management
<i>FC</i>	Fuel Cell
<i>FCTM</i>	Fuel Cell Thermal Management
<i>HP</i>	Heat Pump
<i>HTC</i>	Heat Transfer Coefficient
<i>ICE</i>	Internal Combustion Engine
<i>LES</i>	Large Eddy Simulation
<i>LMTD</i>	Logarithmic Mean Temperature Difference
<i>MTM</i>	Motor Thermal Management
<i>PTC</i>	Positive Temperature Coefficient
<i>RANS</i>	Reynolds Averaged Navier-Stokes

## Symbols

$\alpha$	Thermal Diffusivity [ $m^2/s$ ]
$\delta_{ij}$	Kronecker Delta Function
$\dot{m}$	Mass Flow [ $kg/s$ ]
$\mu$	Dynamic Viscosity [ $Pa \cdot s$ ]
$\nu_T$	Kinematic Eddy Viscosity
$\nu$	Kinematic Viscosity [ $m^2/s$ ]
$\rho$	Density [ $kg/m^3$ ]

$A$	Area [ $m^2$ ]
$c_p$	Specific Heat Capacity [ $J/(kg \cdot K)$ ]
$g$	Gravitational Acceleration [ $m/s^2$ ]
$h$	Heat Transfer Coefficient [ $W/(m^2 \cdot K)$ ]
$k$	Thermal Conductivity [ $W/(m \cdot K)$ ]; Turbulence Kinetic Energy [ $J$ ]
$L$	Length [ $m$ ]
$Nu$	Nusselt Number
$P$	Pressure [ $Pa$ ]
$Pr$	Prandtl Number
$q$	Heat Transfer [ $W$ ]
$q''$	Heat Flux [ $W/m^2$ ]
$R$	Thermal Resistance [ $K/W$ ]
$r$	Radius [ $m$ ]
$Re$	Reynolds Number
$T$	Temperature [ $K$ ]
$t$	Time [ $s$ ]
$u, v, w$	Velocity in x, y, z directions [ $m/s$ ]

# 1 Introduction

## 1.1 Background

Global warming and climate change problems caused by rise in consuming fossil fuels has resulted in growth in development of zero tailpipe emissions vehicles. An important development towards ecofriendly transportation is electric vehicles (EV) [1,2]. Even with their increased efficiency and zero tailpipe emissions, EVs powered by batteries still face challenges with safety, range, cost, and low battery performance in extreme temperatures. The main reason behind the slow growth of EVs in the market is their vehicle range. While increasing an EV's battery capacity can extend its range, doing so may also result in an increase in the vehicle's weight, volume, and cost [1,3]. Reducing the power consumption of EVs' climate system is an alternative method. This can be accomplished in two ways: by making the air conditioning (AC) system more efficient and by lowering the climate control load in EVs. Consequently, researchers and automakers have given electric vehicle thermal management (EVTM) solutions high attention. As vehicle electrification and knowledge progress, these systems strive for optimal operating temperatures and enhance energy utilization efficiency [3,4].

In vehicles with internal combustion engines (ICE), the ability to meet the heating capacity is typically taken for granted in cold climates because there is always enough waste heat from the engine. For EVs in cold climates, however, the heating objective needs to be carefully chosen to achieve high efficiency, since there is no waste heat from engines. Furthermore, Therefore, additional energy is often required that can be provided by a positive temperature coefficient (PTC) heater and a heat pump (HP) system [2, 4, 5, 6, 7]. The AC system in EVs uses a significant amount of battery power to heat and cool the cabin to enhance passenger thermal comfort, significantly reducing the EVs' driving range. This suggests that maintaining a high enough temperature inside EV cabins may be a significant factor in decreasing driving range. As was previously noted, PTC is widely used for cabin heating. PTC-based electric heater systems can be installed at low costs, but because they rely on electric conversion, they consume a lot of battery power when in use, drastically reducing the range of the vehicle [1].

In contrast to PTC heaters, HP systems enhance heating efficiency by transforming atmospheric heat. HP systems can also utilize the limited waste heat from the electric motor or the battery to support the cabin heating or dehumidification process. At an ambient temperature of  $-7^{\circ}\text{C}$ , the coefficient of performance (COP) of HP systems with the same system components is close to 2 [5]. By this COP value HP system can provide heat to the cabin double the amount of consumed electricity. At an ambient temperature of  $-10^{\circ}\text{C}$ , it was observed that the driving range of the electric vehicle with HP heating increased by 23% compared to that with PTC heating [6]. However, a disadvantage of the HP system is that as the outside temperature lowers, its heating capability drastically decreases as well [2, 5]. This is one of the main challenges for optimization of thermal system in extreme weather conditions. The choice of the heat source in the EVs thermal system is dependent on various circumstances but HP system appears to be a promising choice for future thermal management systems. The heat source can be used in each of thermal systems in EV or somehow integrate them. For this, first EVs thermal management systems should be introduced.

The three primary systems that make up the battery electric vehicle (BEV) thermal management are battery thermal management (BTM), motor thermal management

(MTM), and cabin thermal management (CTM), which are responsible for power batteries, electric motors (EM), and cabins on an EV [6]. In Here, BTM, MTM, CTM and the integrated thermal management system are explained.

### **1.1.1 Battery thermal management (BTM)**

The electrochemical process produces a lot of heat inside the battery, which may cause the temperature to rise quickly, negatively impacting its functioning efficiency, and possibly even result in safety issues [2]. Also, the batteries operating in extremely hot temperatures experience a decline in performance [4]. On another way, due to the battery's deterioration during low-temperature operation, EVs are less competitive with ICE vehicles in places with cold climates. Many methods for preheating batteries before and while charging or usage have been suggested to lessen the effect of winter ambient temperature on batteries [1]. Battery thermal management can be divided into three categories: liquid, phase change material (PCM), and air cooling. The selection of coolant and cooling mode, geometric structure optimization, flow rate and direction control, etc. are the primary areas of current research attention. For both summer cooling and winter preheating, the liquid-based cooling method is suitable. Liquid-based cooling methods are currently commonly used by EV manufacturers, particularly in BEVs, due to their high cooling capability and reliability. However, it should be mentioned that EVs using BTM with liquid cooling need additional components, including a heat exchanger and pump [1, 4, 6]. Many liquid-cooling BTMs use the water-glycol mixture because it reduces the freezing point [6]. Using these usual methods, the cooling capacity of the battery temperature control system must be set high enough to prevent the battery from reaching an excessively high temperature resulting in an oversized thermal management system [2].

### **1.1.2 Motor thermal management (MTM)**

The growing popularity of electric vehicles raises the need for highly efficient and high power-density electric motors, which increases the amount of heat produced in the motor's limited effective cooling space [4]. The two most popular cooling techniques for motor cooling are liquid and air cooling. Liquid cooling has a higher specific heat than air cooling and has the ability to independently change the system temperature as needed. Liquid cooling may efficiently address the heat dissipation issue of high-power motors and enhance the efficiency and lifespan of the motor, power electronics, and other components of new energy vehicles. Electrical motors can also be cooled by lubricating oil. The motor thermal management (MTM) that uses liquid is more efficient than one that uses air because liquid has a higher heat transfer coefficient [4,6]. Water's high heat capacity and low cost make it the most popular coolant for EMs in EVs. The water-based MTM is more efficient than the oil-based one for the same channel configuration [6].

### **1.1.3 Cabin thermal management (CTM)**

Most of electric vehicles use AC system to keep the cabin cool. Typical components of an EV's AC system are a compressor, two blowers, an evaporator, a condenser, and an expansion valve. The evaporator and an additional blower are situated within the cabin, but the condenser and one of the blowers are situated outside. PTC heaters and HPs are the most common cabin heating options for pure EVs; with PCM as an alternative [6].

### 1.1.4 Integrated thermal management system

The significance of EV thermal management systems is increasing due to the advancements in vehicle electrification and knowledge. These systems ensure that functional units operate at the ideal temperature and enhance the vehicle's energy efficiency. The cabin, battery, motor, and power electronics in typical thermal management system solutions are independent and managed in different ways, resulting in a complicated system with many pipes and components, limited collaboration, and high-power consumption [4]. An electric vehicle's integrated heating system for both the cabin and the battery could be used to solve the issue of the heating system's battery-power consumption at lower ambient temperatures. Multiple thermal management systems are combined into an organic whole by the integrated thermal management solution. Maximizing a systematic design is only possible by combining the needs and applications of every thermal management system into one integrated system. In order to encourage the popularity of EVs in extreme climate conditions, integrated thermal management systems are a crucial and necessary step [1, 4, 6, 7].

## 1.2 Previous studies

Water glycol mixture coolant is usually used for ED system cooling and BTM system [8]. The Coolant flows between different components in EV under-hood via coolant hoses and a fan is used to flow air into the coolant heat exchanger and thereby remove heat from the coolant circuit in EV under-hood.

In the work done by Shim and Park [9], a transient analytic technique was applied to engine cooling and under-floor heat protection during vehicle development. The research examines cooling performance and thermal damage, particularly post-ignition-off after uphill driving, using CFD codes Star-CCM+ and RadTherm. The method provides precise estimates of temperature distribution and variations over time and has been tested against wind tunnel testing.

Ljungskog and Nilsson [10] have compared two approaches with various meshing techniques in order to estimate the development of a highly automated CFD model for under-hood compartments. They have developed two methods with different mesh settings utilizing STAR-CCM+ for CFD analysis. The method with polyhedral mesh has indicated higher efficiency and better convergence than the other one but both methods have underpredicted the heat rejection considering the validation tests, which calls for deeper investigation and complete validation in these methods.

This coolant hoses can be influenced by excess heat released from each of the components which is addressed as heat pick up. Borg and Owen [11] in a thesis work investigated heat pickup in vehicle cooling system hoses, examining its impact on coolant temperature due to temperature variations in the under-hood compartment. Experimental measurements and CFD modeling were employed to quantify the phenomenon's effects and improve the accuracy of 1 dimensional CFD modeling for the entire cooling system.

Conversely, fan air flow can also have a side effect on coolant hoses. The air flow in EV under-hood can cause convective heat loss from coolant hoses. The heat loss caused by fan flow can impact the cooling system performance and reduce its efficiency. By

quantifying the heat rejected from each coolant hose, the impact of this energy loss on total energy efficiency of EV will be indicated.

The convective heat transfer between flow in the pipe and air cross flow over the pipe has been investigated in many studies. Hatton et al. [12] presented experimental findings on mixed convection regime around electrically heated cylinders, which covered a wide range of forcing velocities and temperature differences. He proposed correlations for forced and natural convection conditions, with an additional correlation acquired for combined forced and natural convection regions, showing good agreement with experiments.

Despite all the studies in the area of convective heat transfer from pipes affected by cross sectional air flow, there is limited research in the area of heat loss from coolant hoses which are affected by air flow in vehicle under-hood area. This topic is the focus of this study. It is intended to quantify and predict the heat loss from coolant hoses affected by air flow by simulations. The results can later be used for improving thermal 1 dimensional modeling.

### **1.3 Objective**

For the specific case of this study based on the material of hose, the temperature of the coolant and fan flow rate, heat loss of each hose has a low order of magnitude that cannot be distinguished from the measurement error. This issue makes it difficult to determine the convective heat losses of coolant hoses in the complete vehicle tests. Therefore, a simplified rig is utilized to mimic the same process with modified conditions. In this study it is intended to provide a comprehensive CFD comparable with experimental results from the simplified rig by analyzing the influence of key factors.

## 2 Theory

In this section the relevant theory for heat loss prediction in coolant hoses is briefly explained. It is important to have a good understanding of the fundamental relations in both areas of fluid dynamics and heat transfer to be able to conduct them properly. In this case the main reason is to predict heat loss. Numerical methods used for simulation is also described in this section.

### 2.1 Heat transfer

Fundamentals of heat transfer are important in understanding of the heat loss from coolant flow inside the hoses to the under-hood air flow. According to the basis of the heat transfer, heat is transferred between two media if there is a temperature difference between them [13]. And heat is always transferred from medium with high temperature to medium with low temperature. Heat can be transferred by three types of conduction, convection, and radiation. In case of heat loss from coolant hoses we only consider the two types of conduction and convection and in the following sections, each of them is explained in more detail.

#### 2.1.1 Conduction

The transfer of energy to the less energetic molecules or particles from more energetic molecules or particles in a substance due to the interactions between them is called conduction. Higher temperature results in higher energetic particles and the interactions like collisions between particles results in transfer of energy between them. With a temperature gradient in the substance, the direction of energy transfer is always to the decreasing temperature side. Heat transfer rate in conduction can be calculated by Fourier's law. Equation (2.1) shows the one dimensional conduction heat transfer.

$$q_x'' = -k \frac{dT}{dx} \quad (2.1)$$

$q_x''$  ( $W/m^2$ ) is the heat transfer rate in the x direction divided by the cross-sectional area of the heat transfer.  $\frac{dT}{dx}$  is the temperature gradient in x-direction and it is related to the heat transfer rate by  $k$  ( $W/m.K$ ) as conductivity of each material. The minus sign is to show that the direction of heat transfer is the opposite of temperature gradient (in the direction of decreasing temperature).

Considering heat flux as a vector with components in all directions, we can write Fourier's law in a general statement.

$$\mathbf{q}'' = -k\nabla T = -k \left( \mathbf{i} \frac{dT}{dx} + \mathbf{j} \frac{dT}{dy} + \mathbf{k} \frac{dT}{dz} \right) \quad (2.2)$$

$\frac{dT}{dx}$ ,  $\frac{dT}{dy}$  and  $\frac{dT}{dz}$  are temperature gradients in direction of x, y and z respectively. Heat flux in each direction is perpendicular to the isothermal plane.

#### 2.1.2 Convection

Based on the nature of the flow, convection heat transfer can be classified into two groups. If the flow is caused by external means like fan or pump, the heat transfer is referred as forced convection. On another way, natural convection is caused by buoyancy

forces which are the result of the density gradient induced by temperature difference. But for both of the convectional heat transfer types, the equation (2.3) is used to calculate the heat transfer flux.

$$q'' = h(T_s - T_\infty) \quad (2.3)$$

This equation is known as Newton's law of cooling.  $q''(W/m^2)$  is heat flux perpendicular to the surface of heat transfer and according to the equation it is proportional to the temperature difference between  $T_s(K)$  as surface temperature and  $T_\infty(K)$  as the fluid temperature, and  $h(W/m^2.K)$  as convective heat transfer coefficient. This coefficient is dependent to the nature of the fluid, fluid motion and surface properties.

### 2.1.3 Heat transfer relations

Based on the first law to thermodynamics for steady state in a controlled volume, the amount of thermal and mechanical energy generated within the control volume is equal to the amount of thermal and mechanical energy leaving the control volume minus the amount of thermal and mechanical energy entering the control volume. This law can be shown in equation (2.4).

$$\dot{m} \left( u_t + pv + \frac{1}{2}V^2 + gz \right)_{in} - \dot{m} \left( u_t + pv + \frac{1}{2}V^2 + gz \right)_{out} + q - W = 0 \quad (2.4)$$

Each term within the parentheses represents the forms of energy (thermal, fluid work, kinetic and potential) per unit mass flow rate of inlet and outlet. Enthalpy per unit mass ( $h(J/kg)$ ) can be used instead of sum of thermal energy and fluid work per unit mass.

$$h = u_t + pv \quad (2.5)$$

Neglecting changes in latent energy between inlet and outlet mass flow as well as considering the fluid as ideal gas, enthalpy difference can be replaced with  $(h_{in} - h_{out}) = c_p(T_{in} - T_{out})$  in which  $T_{in}$  and  $T_{out}$  are temperatures in inlet and outlet and  $c_p$  is the specific heat capacity at constant pressure. In the case where fluid is an incompressible fluid, the specific heat capacity at constant pressure and constant volume can be considered equal. Flow work can also be neglected by not having large pressure differences in the flow. By neglecting changes in kinetic and potential energy in inlet and outlet flow, the simplified steady state thermal equation can be achieved.

$$q = \dot{m}c_p(T_{out} - T_{in}) \quad (2.6)$$

Where  $q(W)$  is the thermal power given to the control volume which is proportional to the temperature difference between inlet and outlet,  $\dot{m}(kg/s)$  as mass flow rate of inlet and outlet flow and  $c_p(J/kg.^\circ K)$  as specific heat capacity for the fluid. This equation is only valid for ideal gases and incompressible fluids.

### 2.1.4 Thermal resistance

The heat transfer from each heat transfer types can be also expressed in equation (2.7).

$$q = q'' A = \frac{\Delta T}{R_t} \quad (2.7)$$

$A(m^2)$  is the area perpendicular to the heat transfer direction and  $\Delta T$  is the temperature difference between the two media in contact.  $R_t$  is defined as thermal resistance which has different forms in each heat transfer type. Based on equation (2.1), thermal resistance for conduction in a plane wall is shown in equation (2.8).

$$R_{t,cond} = \frac{T_{s,1} - T_{s,2}}{q_x} = \frac{L}{kA} \quad (2.8)$$

In equation (2.8),  $T_{s,1}$  and  $T_{s,2}$  are surface temperatures in each side of the wall and  $L(m)$  is the length of the wall. This thermal resistance is defined the same as Ohm's law for electrical conduction. Using this method will simplify complicated heat transfer problems. This thermal resistance can also be defined for other types of heat transfer. Based on equation (2.3), thermal resistance for convection is defined as following:

$$R_{t,conv} = \frac{T_s - T_\infty}{q} = \frac{1}{hA} \quad (2.9)$$

In case of this study, a brass pipe is exposed to coolant flow from inner side of the pipe and cross air flow from outer side of the pipe. The conduction heat transfer is in radial direction and the thermal resistance will be in the form of:

$$R_{t,cond} = \frac{\ln(r_2/r_1)}{2\pi Lk} \quad (2.10)$$

Where  $L$  is the length and  $r_2$  and  $r_1$  are the outer and inner diameter of the pipe respectively.

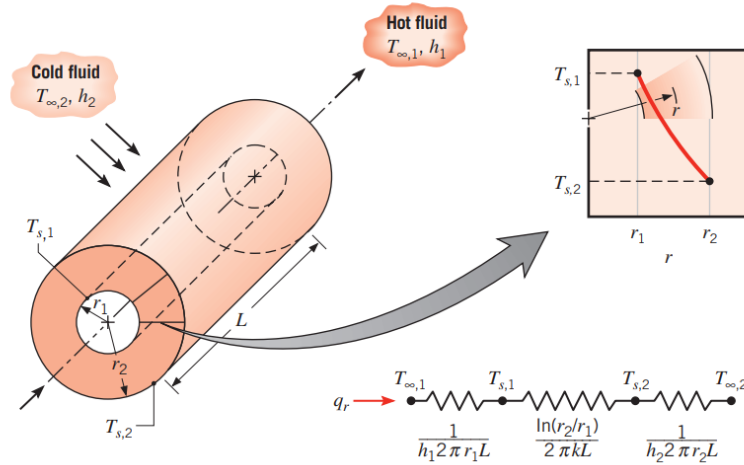


Figure 2.1 Series of thermal resistances between cross air flow and fluid in the pipe [13]

Considering each medium's thermal resistance in equivalent thermal circuit, all the resistances will be in series which can be seen in Figure 2.1. Total equivalent can be calculated by summing all the thermal resistances.

$$R_{tot} = \frac{1}{h_1 A_1} + \frac{\ln(r_2/r_1)}{2\pi k L} + \frac{1}{h_2 A_2} \quad (2.11)$$

We can replace  $R_{tot}$  with the overall heat transfer coefficient:

$$UA = \frac{1}{R_{tot}} \quad (2.12)$$

By this overall heat transfer can be calculated by equation (2.13):

$$q_{tot} = UA\Delta T \quad (2.13)$$

Where  $\Delta T$  is the temperature difference between air flow and coolant flow in our case. Equation (2.13) can be used locally but not for the whole pipe.

## 2.1.5 Convective heat transfer coefficient

In order to calculate the overall heat transfer coefficient ( $U(W/m^2.K)$ ), first convective heat transfer coefficient ( $h$ ) must be calculated for air and coolant flow. In this case Nusselt number which is defined as the ration between convective and conductive heat transfer is used.

$$Nu = \frac{q_{conv}}{q_{cond}} = \frac{hL}{k} \quad (2.14)$$

This equation is also used with surface averaged heat transfer coefficient to calculate average Nusselt number. This dimensionless number is used for measuring convective heat transfer rate at the surface and is usually correlated by fluid flow's Reynolds number ( $Re_L$ ) and Prandtl number ( $Pr$ ). Many empirical correlations have been suggested to calculate Nusselt number according to the fluid's Prandtl and Reynolds number. These correlations differ according to the shape of the surface or range for Reynolds number of fluid flow. One of the suggested correlations by is as follows [13].

$$Nu_D = \frac{(f/8)(Re_D - 1000)Pr}{1 + 12.7(f/8)^{1/2} ((Pr^{2/3}) - 1)} \quad (2.15)$$

Equation (2.15) can be used for internal flows in circular tubes. For the flows in the range of  $0.5 \leq Pr \leq 2000$  and  $3000 \leq Re_D \leq 5 \times 10^6$ , this correlation is valid. This correlation can be used for coolant flow in the pipe.  $f$  is the friction factor and is calculated by equation (2.16):

$$f = (0.790 \ln Re_D - 1.64)^{-2} \quad 3000 \leq Re_D \leq 5 \times 10^6 \quad (2.16)$$

In equation (2.17), a correlation is suggested for Nusselt number in cross sectional external flows over circular cylinder.

$$Nu_D = C Re_D^m Pr^n \left( \frac{Pr}{Pr_s} \right)^{1/4} \quad (2.17)$$

Coefficients of  $C$  and  $m$  are listed in table 1.1 for different Reynolds numbers. External flow temperature is used for evaluation all the properties except for  $Pr_s$  which is evaluated at cylinder surface temperature. If  $Pr \lesssim 10$ ,  $n = 0.37$ ; if  $Pr \gtrsim 10$ ,  $n = 0.36$ .

Table 2.1 Coefficients for equation (2.17) [13]

$Re_D$	$C$	$m$
1 – 40	0.75	0.4
40 – 1000	0.51	0.5
$10^3 - 2 \times 10^5$	0.26	0.6
$2 \times 10^5 - 10^6$	0.076	0.7

## 2.1.6 Energy balance

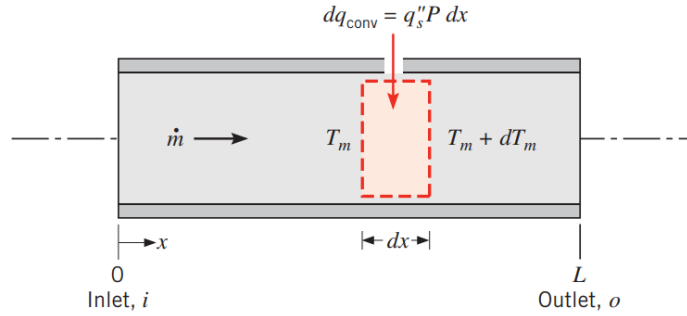


Figure 2.2 Energy balance of in a pipe cross sectional control volume [13]

For simplifying the energy balance in the circular pipe cross sectional element according to Figure 2.2, some energy transfers can be neglected. For example, heat transfer in axial direction can be neglected and the fluid can be modelled as a incompressible or ideal gas and pressure variations can be neglected. With all the simplifications, the energy balance will be as equation (2.1). This equation for the control volume shown in the picture can be rewrite as:

$$\frac{dT_m}{dx} = \frac{q_s'' P}{m c_p} = \frac{P}{m c_p} h(T_s - T_m) \quad (2.18)$$

Where  $P$  in the perimeter of the cylinder and  $q_s''$  is the heat flux to the internal flow in the control volume. Based on the location of surface temperature ( $T_s$ ), heat transfer coefficient can be either for only for the internal flow or for series of internal flow and the pipe wall. By considering the external flow heat transfer coefficient in series,  $T_s$  can be replaced with air temperature ( $T_\infty$ ). In the condition of constant  $T_\infty$ , by defining  $\Delta T = T_\infty - T_m$  the equation can be rewritten as  $-\frac{d(\Delta T)}{dx} = \frac{P}{m c_p} h \Delta T$ . By solving this equation from inlet to outlet of the pipe, equation (2.19) is achieved.

$$\ln \frac{\Delta T_o}{\Delta T_i} = \ln \frac{T_\infty - T_{m_o}}{T_\infty - T_{m_i}} = -\frac{PL}{m c_p} \bar{h} \quad (2.19)$$

Based on the definition of average heat transfer coefficient  $\bar{h} = \frac{1}{L} \int_0^L h dx$ , local heat transfer coefficient ( $h$ ) in equation (2.19) is replace with average heat transfer coefficient ( $\bar{h}$ ).  $T_{m_o}$  and  $T_{m_i}$  are internal flow's outlet and inlet temperature respectively. By this definition, total heat transfer between external flow and internal flow which is the same as heat transfer gained by internal flow will be:

$$q = m c_p (T_{m_o} - T_{m_i}) = m c_p ((T_\infty - T_{m_i}) - (T_\infty - T_{m_o})) = m c_p (\Delta T_i - \Delta T_o) \quad (2.20)$$

By replacing equation (2.19) in equation (2.20), we can reach equation (2.21):

$$q = \bar{h} A_s \Delta T_{lm} \quad (2.21)$$

Pipe surface is calculated by  $A_s = P.L$ . log mean temperature difference ( $\Delta T_{lm}$ ) is calculated based on:

$$\Delta T_{lm} = \frac{(\Delta T_o - \Delta T_i)}{\ln \frac{\Delta T_o}{\Delta T_i}} \quad (2.22)$$

## 2.2 Fluid dynamics

In order to simulate heat transfer phenomena, fluid dynamic phenomena should also be considered. These two phenomena are coupled and solved together. Governing equations [11] in fluid dynamics are explained here.

$$\frac{\partial u_i}{\partial x_i} = 0 \quad (2.23)$$

Equation (2.23) is the equation for conservation of mass for incompressible fluid.  $u_i$  is the velocity and  $x_i$  is the spatial coordinate.

$$\frac{\partial u_i}{\partial t} + u_j \frac{\partial u_i}{\partial x_j} = -\frac{1}{\rho} \frac{\partial P}{\partial x_i} + \nu \frac{\partial^2 u_j}{\partial x_j \partial x_j} \quad (2.24)$$

Equation (2.24) is the conservation of momentum equation for incompressible fluids. This form of the equation is known as Navier Stokes equation and  $\nu$  is the kinetic viscosity.

$$\rho C_p \frac{DT}{Dt} = -\nabla(-k\nabla T) - p\nabla \cdot \mathbf{u} + \Phi \quad (2.25)$$

Equation (2.25) is the conservation of energy equation where  $\Phi$  is the heat dissipation and  $k$  is the conductivity of the fluid.  $\rho$ ,  $C_p$  and  $p$  are fluid's density, specific heat capacity and pressure respectively.  $\Phi$  is defined as:

$$\Phi = \frac{1}{2} \left( \frac{\partial u_i}{\partial x_j} + \frac{\partial u_j}{\partial x_i} \right)^2 \quad (2.26)$$

Equation (2.25) is showing heat loss from dissipation and conduction from the fluid must equal the net energy convection into the fluid.

In order to be able to solve these equations for turbulent flow, first we should have a good understanding of the turbulent flow itself. The chaotic behavior and variations in pressure and velocity are typical characteristics of turbulent flows. By utilizing Reynold decomposition to the pressure and velocity of the fluid in the Navier Stokes equations, the governing equations can be adjusted to turbulent flow characteristics. In Reynolds decomposition velocity and pressure are decomposed to mean and fluctuation values.

$$u = \bar{U} + u' \quad (2.27)$$

$$p = \bar{P} + p' \quad (2.28)$$

By applying these decompositions and time averaging on Navier Stokes equations, Reynolds Averaged Navier-Stokes (RANS) equation will be obtained:

$$u_j \frac{\partial \bar{u}_i}{\partial x_j} = -\frac{1}{\rho} \frac{\partial}{\partial x_i} (-\bar{P} \delta_{ij} + 2\mu S_{ij} + \tau'_{0ij}) \quad (2.29)$$

- $\delta_{ij}$  is the Kronecker delta.
- $S_{ij}$  represents the mean strain-rate tensor.
- $\tau'_{0ij}$  represents the Reynolds stress tensor.

## 2.2.1 Computational fluid dynamics

Nowadays in both industry and academia, computational fluid dynamics (CFD) which relies on numerical techniques is frequently used to study complex flow phenomena. CFD simulations can help us in predicting the behavior of the flow in different condition which can be hard and expensive to experiment them [14]. In order to solve the fluids behavior especially turbulent behavior, CFD modeling have been used to simplify the equations.

### 2.2.1.1 Reynolds Averaged Navier Stokes (RANS)

Based on the shown Reynolds Averaged Navier-Stokes (RANS) equations (equation (2.29)), there are many closure models for the RANS equations that can be used to model the turbulent parts, which govern the transport equations of the mean flow quantities. For steady-state scenarios, the averaging procedure can be regarded as time-averaging, and for periodic transient scenarios, as ensemble averaging. Equations for the mean quantities are obtained by replacing the decomposed solution variables into the Navier-Stokes equations. By replacing the variables,  $\tau'_{ij}$  will be added to the parameters as Reynolds stress tensor which defined as:

$$\tau'_{ij} = -\rho \begin{pmatrix} \overline{u'^2} & \overline{u'v'} & \overline{u'w'} \\ \overline{u'v'} & \overline{v'^2} & \overline{v'w'} \\ \overline{u'w'} & \overline{v'w'} & \overline{w'^2} \end{pmatrix} \quad (2.30)$$

Stresses generated by turbulent fluctuations' interactions are indicated by the Reynolds Stress Tensor. This parameter adds a new variable, but the number of equations is still the same which leads to a closure problem. The Boussinesq approximation is used to solve this.

$$-\overline{u'_i u'_j} = 2\nu_T S_{ij} - \frac{2}{3}k\delta_{ij} \quad (2.31)$$

$$k = \frac{1}{2}\overline{u'_i u'_i} \quad (2.32)$$

- $\nu_T$  is the kinetic eddy viscosity.
- $S_{ij}$  is the mean strain rate tensor.
- $k$  is the turbulence kinetic energy.

In order to model the turbulence kinetic energy, different methods have been introduced. Based on the models used in this thesis only two models of Realizable k-epsilon and k-Omega SST are explained. These models differ in modeling of kinetic energy and specific dissipation rate. The specific dissipation rate for each of the models is described as follows:

$$\nu_T = C_\mu \frac{k^2}{\varepsilon} \quad (2.33)$$

$$\nu_T = \frac{k}{\omega} \quad (2.34)$$

Equation (2.33) is for k-epsilon model and equation (2.34) is for k-Omega model. The turbulence and specific dissipation rates are defined by  $\varepsilon$  and  $\omega$  respectively. In k-epsilon model, turbulent kinetic energy and dissipation rate are achieved by these equations:

$$\frac{\partial k}{\partial t} + U_j \frac{\partial k}{\partial x_j} = \tau_{ij} \frac{\partial U_i}{\partial x_j} - \varepsilon + \frac{\partial}{\partial x_j} \left[ \left( \nu + \frac{\nu_t}{\sigma_k} \right) \frac{\partial k}{\partial x_j} \right] \quad (2.35)$$

$$\frac{\partial \varepsilon}{\partial t} + U_j \frac{\partial \varepsilon}{\partial x_j} = C_{\varepsilon 1} \frac{\varepsilon}{k} \tau_{ij} \frac{\partial U_i}{\partial x_j} - C_{\varepsilon 2} \frac{\varepsilon^2}{k} + \frac{\partial}{\partial x_j} \left[ \left( \nu + \frac{\nu_t}{\sigma_\varepsilon} \right) \frac{\partial \varepsilon}{\partial x_j} \right] \quad (2.36)$$

Where  $C_{\varepsilon 1}$ ,  $C_{\varepsilon 2}$ ,  $C_\mu$ ,  $\sigma_k$  and  $\sigma_\varepsilon$  are closure coefficients for the modeling. The equations for turbulent kinetic energy and specific dissipation rate are as follows:

$$\frac{\partial k}{\partial t} + U_j \frac{\partial k}{\partial x_j} = \tau_{ij} \frac{\partial U_i}{\partial x_j} - \beta^* k \omega + \frac{\partial}{\partial x_j} \left[ \left( \nu + \sigma^* \frac{k}{\omega} \right) \frac{\partial k}{\partial x_j} \right] \quad (2.37)$$

$$\frac{\partial \omega}{\partial t} + U_j \frac{\partial \omega}{\partial x_j} = \alpha \frac{\omega}{k} \tau_{ij} \frac{\partial U_i}{\partial x_j} - \beta \omega^2 + \frac{\sigma_d}{\omega} \frac{\partial k}{\partial x_j} \frac{\partial \omega}{\partial x_j} + \frac{\partial}{\partial x_j} \left[ \left( \nu + \frac{\sigma_k}{\omega} \right) \frac{\partial \omega}{\partial x_j} \right] \quad (2.38)$$

$\alpha, \beta, \beta^*, \sigma, \sigma^*$  are closure coefficients for this modeling. But other improvements have also been made to these two models to make the models more real. k-epsilon realizable and k-Omega SST are the most widely models in each model respectively.

### **2.2.1.2 Scale resolving CFD methods**

In the Large Eddy Simulation (LES) model [14], the governing equations of fluid motion are solved numerically on a grid, and the large-scale turbulent eddies are directly resolved instead of using the RANS models, while the smaller scales are modeled using sub grid-scale models. By resolving the large-scale motions, LES provides accurate predictions of turbulent flow phenomena, including flow separation, vortex shedding, and turbulent mixing, without the need for excessive grid refinement.

In Detached Eddy Simulation (DES) model, the aspects of Large Eddy Simulation (LES) and Reynolds Averaged Navier-Stokes (RANS) are combined to efficiently simulate turbulent flows. When modeling close to solid boundaries, when fine boundary layer resolution is crucial, DES employs RANS modeling. However, when the flow is detached and large-scale eddies are dominant, LES modeling is used. This makes it especially appropriate for complex flow issues that involve large-scale turbulence and boundary layer phenomena.

### 3 Methodology

This study is aiming to investigate the accuracy of the computational fluid dynamics (CFD) simulations in prediction of heat loss in pipes with high temperature fluid flow affected by external flow air especially in coolant hoses exposed to fan air flow. For this aim a simplified rig is designed to mimic this phenomenon in a larger scale in both experiment and CFD simulation. In this section features of experiment in the rig and the simulation will be explained in detail.

#### 3.1 Experiment

In this part, Geometry of the rig in addition to the measurement system is described and different components are explained.

##### 3.1.1 Geometry

The rig consists of a  $1.5\text{ m} \times 1\text{ m} \times 0.5\text{ m}$  wooden box which a suction fan is installed in one side and the opposite side is open. A 1 m long brass pipe with outer diameter of 20 mm and 2 mm thickness is installed in the box perpendicular to the flow caused by the fan. A nozzle is installed in the open side of the box to reduce the effect of box edges on the fan flow in the box. Details of the rig can be seen in Figure 3.1.

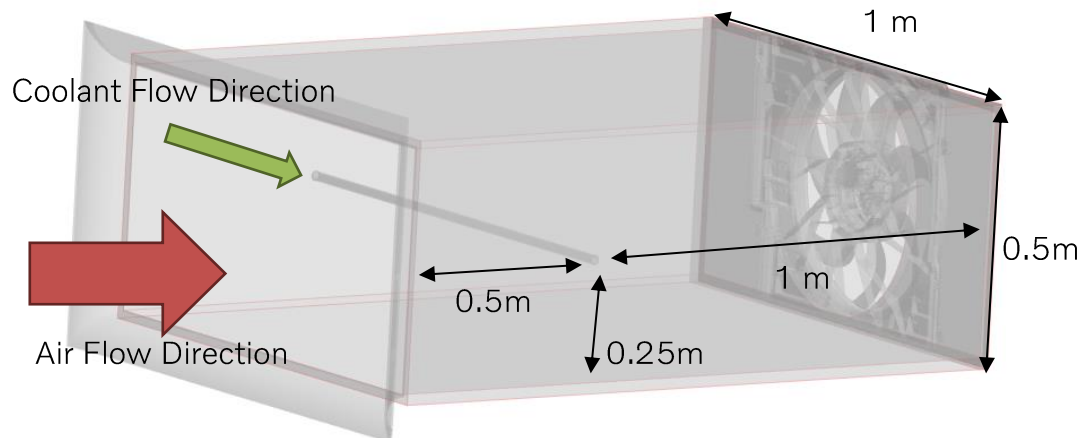


Figure 3.1 Geometry specifications of the rig

Coolant flows in the brass pipe by an external flow circuit controlled by a pump and valves. Coolant used in this experiment is 50 % (v/v) ethylene glycol/water mixture. The coolant pump utilized in the rig is not designed to produce the low flow rate range required in the test, hence a bypass circuit is added to the coolant flow circuit and by adjusting both box valve and bypass valve from Figure 3. 2, pump runs at a stable flow and a small portion is led to the box pipe. Air flow is also controlled by the fan rotation rate.

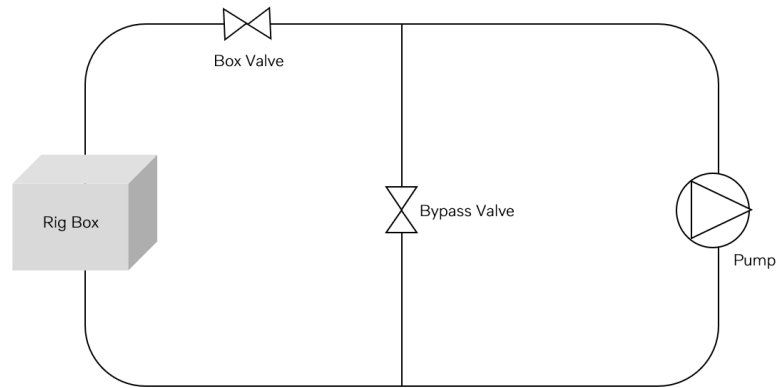


Figure 3.2 Coolant circuit

### 3.1.2 Measurement

In order to capture the heat loss properly, measurement devices must be chosen according to the required accuracy and measurement range of the experiment. For this reason, based on the experiment, measurement devices for measurement of temperature, flow speed and flow rate are used. Each of the chosen devices will be explained in the following parts.

#### 3.1.2.1 Temperature measurement

In order to determine the heat transfer between air and coolant flow, temperature measuring sensors are needed both for air and coolant side. Thermocouple temperature sensors are used for measuring air temperature entering the box. Since heat loss is obtained from the temperature difference between coolant flow's inlet and outlet, PT100 temperature sensors with a higher accuracy than thermocouples are used.

##### 3.1.2.1.1 Thermocouple temperature sensors

Thermocouples are one of the most popular temperature sensors. In addition to their low cost, they are also reliable and have a wide measuring range which can be used in many different experiments. While thermocouples are widely used, it is difficult to obtain accuracy much better than 1°C with them [15]. However, because of their many benefits, they continue to be the widely used type of sensor for industrial measurements today. Thermocouples operate on the principle of the Seebeck effect, which states that a pair of different metals in contact with one another at each end would produce a very small electrical potential when exposed to changes in temperature. Therefore, in a thermocouple temperature change can be detected when two dissimilar metals in contact produce electrical voltage. Based on the low cost and their availability, 6 thermocouples are used to measure air temperature at the inlet of the box. These 6 thermocouples can be used to compare temperature pattern of air with simulations.

##### 3.1.2.1.2 PT100 temperature sensors

PT100 temperature sensor is an RTD (Resistance Temperature Detector) which within its range is typically more linear, drift-free and more accurate than a thermocouple [16]. Nevertheless, they cost more than thermocouples because of their platinum content and more complicated production process. RTDs operate by using the electrical resistance

principle, as in contrast to thermocouples, which are passive sensors. To quantify a change in resistance, a small current must be passed through them. The basis for RTDs' operation is the concept that some metals have a highly precise and stable relationship between resistance and temperature. We can determine the temperature change by measuring this resistance change. Temperature ranges and accuracy level are different between metals. Platinum is most popularly used metal in RTDs and in PT100, "PT" stands for platinum and "100" stands for 100 $\Omega$  as the resistance at 0 °C. Based on the required high accuracy in coolant flow, 3 PT100s in the inlet and 3 PT100s in the outlet are used.

### **3.1.2.2 Magnet flowmeter**

In a magnetic or an electromagnetic flowmeter, the flow is measured by the combination of a sensor and transmitter [17,18]. For the purpose of measuring flow, a magnetic flowmeter uses two electrodes and a set of coils. An applied current from the transmitter powers the meter's coils. Both coils create a magnetic field when powered. Once the pipe is filled and the fluid starts to flow, the fluid's negatively and positively charged particles separate as they move through the magnetic field due to the force of the magnetic field. A voltage is generated between the electrodes and the sensor based on separation. Transmitters receive voltage from sensors, translate it into a flow measurement, and then send the flow measurement to a control system. This flowmeter is used to measure the coolant flow rate before the brass pipe in the box. This flowmeter device is of a high importance since it has a direct effect on the heat loss. SIEMENS SITRANS F M MAG 1100 F magnetic flowmeter is chosen based on its high accuracy in the required range of the coolant flow.

### **3.1.2.3 Hot wire probe**

Hot wire probe or hot wire anemometer is used to measure the air velocity in this experiment. In this probe, a very thin wire that is electrically heated to a temperature higher than the surrounding air [19]. The wire cools when air passes through it. There is a relationship between the resistance of the wire and the flow speed since the electrical resistance of most metals is temperature dependent. By this relation velocity of the air can be measured. Two hot wire probes are used in this experiment to measure the air speed downstream of the pipe. Using of two hot wire probes can be helpful in understanding the air flow distribution better.

## **3.1.3 Measurement system setup**

The location of each measuring device in the rig can be seen from Figure 3. 3 to Figure 3.7. To minimize the heat loss between the temperature measurement point and the test section, hoses in the distance between PT100s and the box are fully insulated and upper part of the PT100s are also insulated in order to minimize the effect of external air flow on their measurement. After installation of all the measurement devices based on the complexity of the room where the rig is located, a study is done on room conditions to achieve a stable air flow in the test section.



*Figure 3.3 Rig setup: Fan and box*

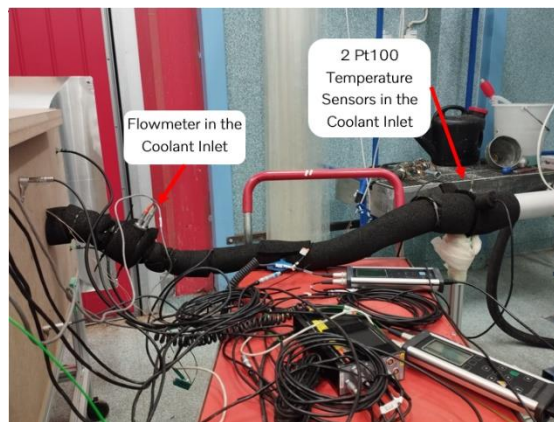


*Figure 3.4 Rig setup: Inlet*

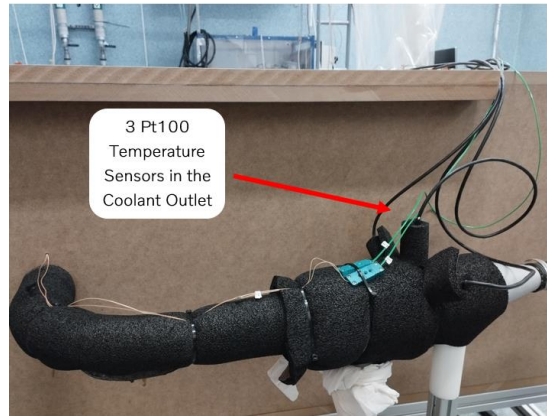


Figure 3.5 Rig setup: Outlet

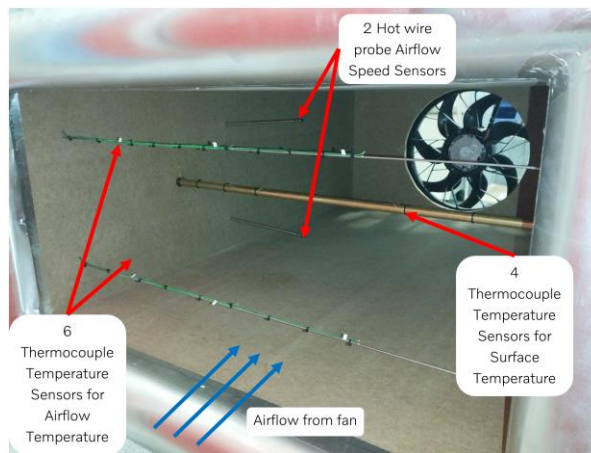


Figure 3.6 Rig setup: Inside the box

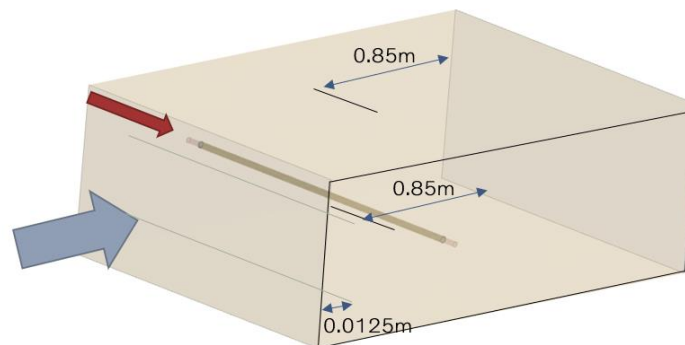


Figure 3.7 Configuration of measurement devices

### 3.1.4 Study of experiment environment

In order to have a uniform heat transfer over the pipe inside the box, a uniform and steady air flow with low fluctuations is needed over the pipe. For this reason, a suction fan was installed at the end of the box to suck the air over the pipe and provide more uniform flow than a blowing fan. six thermocouples in a plane 12.5 cm from the inlet of the box and a hot wire probe were installed according to the geometry to measure

the air flow temperature and velocity respectively. These measurements also provide us with the stability of data over time and from data fluctuations of each we find out the stability of air flow.

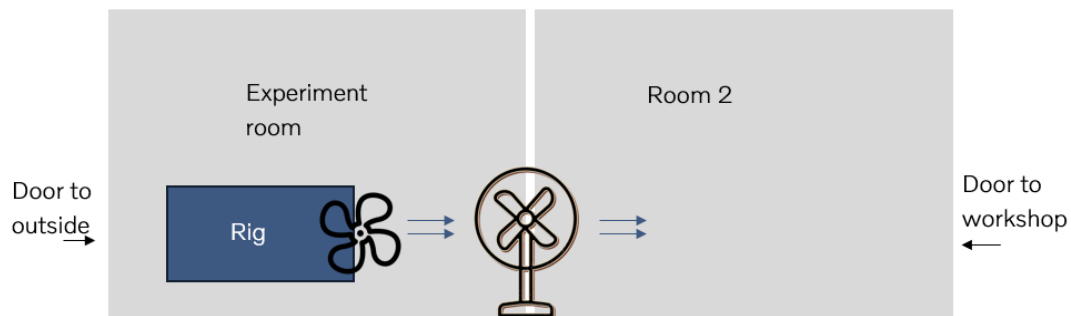


Figure 3.8 Schematic picture of the room where rig is located

The box according to Figure 3.8 is located in the experiment room which has two doors (a door to outside and a door between experiment room and room 2). The first test was conducted when the door between two rooms was closed, no additional fan was used, and the outside door was open to have the outside air temperature on the pipe. The results of thermocouple sensors and only one hot wire sensor in the top can be seen in Figure 3.9.

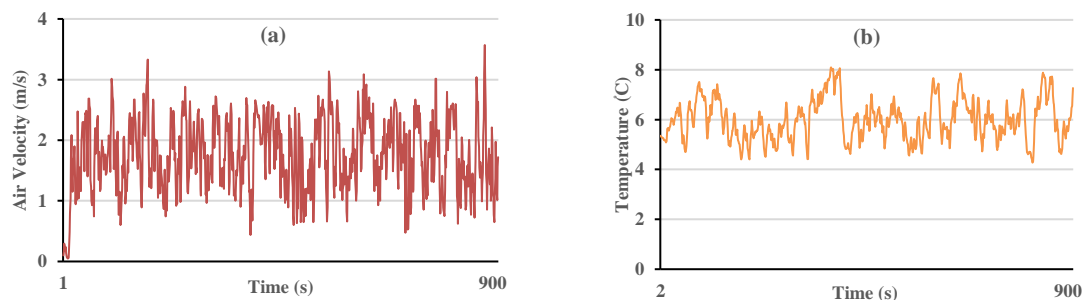


Figure 3.9 (a) Air velocity in the upper hot wire probe and (b) thermocouples average temperature during test before environment study

Based on the data extracted from the first test, the standard deviation of average thermocouple sensors and air flow sensor are  $0.83\text{ }^{\circ}\text{C}$  and  $0.60\text{ m/s}$  respectively which are relatively high and need to be reduced.

Four other cases in addition to main case with different room conditions were introduced to see their effect on the air temperature and velocity fluctuations. The five cases are described below:

- A. The outside door is open, and the rig is located 50 cm outside the outside door. No additional fan is used, and the door between experiment room and room 2 is closed.
- B. The outside door is open, and the rig is located 20 cm inside the outside door. A large suction fan is located between experiment room and room 2, but the next door to the workshop is closed.

- C. The outside door is closed, and the rig is located 20 cm inside the outside door. A large suction fan is located between experiment room and room 2, and the next door to the workshop is open.
- D. The outside door is open, and the rig is located 20 cm inside the outside door. A large suction fan is located between experiment room and room 2, and the next door to the workshop is open.
- E. All doors are closed, and the large fan is not working.

For the mentioned cases, standard deviation of average air temperature from thermocouples and air velocity from hot wire probe in the top is used as a comparison index. The results can be seen in Figure 3. 10.

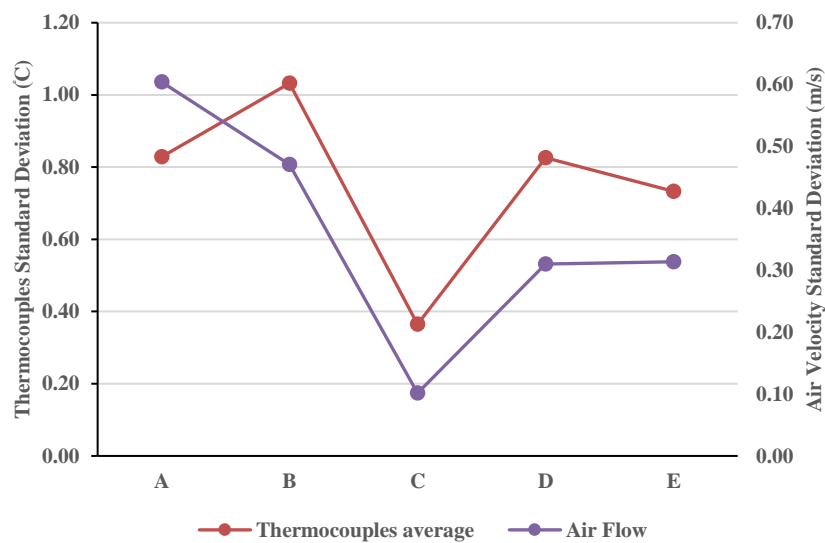


Figure 3.10 comparison of standard deviation of air velocity and thermocouples average during test between room conditions cases

Based on the results we can see that the Case C has the lowest standard deviation both for average temperature and velocity. Therefore, Case C is chosen to be the room condition for all the cases.

### 3.1.5 Test cases

After setting up the rig and installation of all the measurement system, the properties and conditions of test cases must be decided. According to the main target of this study, the test conditions must be chosen to mimic realistic coolant flow conditions in the coolant hoses in car under-hood. On the other way, the setting should be adjusted in a way to increase the heat loss from the coolant pipe to become larger than the uncertainty range of the measurement devices. By this, the comparison between experiment and simulation results will be more reliable and more helpful to understand the level of accuracy of the simulation results. The test cases shown in Table 3.1 are chosen in the lower end of coolant flow range in EVs (0.03-0.4 l/s) to achieve higher temperature drop in the coolant.

*Table 3.1 Test cases' setting properties*

Case Number	Coolant Volumetric flow (l/s)	Temperature Difference between Coolant inlet and Room (°C)	Fan Rotational Speed (rpm)
Case 1	0.050	55	1000
Case 2			1500
Case 3		60	1500
Case 4		65	1000
Case 5			1500
Case 6	0.010	55	1000
Case 7			1500
Case 8		60	1500
Case 9		65	1500

The temperature difference between room and the coolant inlet is chosen based on the fact that during the different dates of the years according to the weather condition, room can have different temperatures. But by using the same temperature difference between room and coolant inlet, we can ensure that the heat transfer rate between air and coolant stays the same neglecting the effect of temperature of the air and coolant properties.

The approximate time to reach each test cases' settings before recording the data is 30 minutes. Data from each test case is recorded for 10 minutes and time averaged results from total 10 minutes of the test is used for comparison and validation with simulation results.

### **3.1.6 Additional improvements to the experiment**

To make sure about the reliability of the experimental results and performance of measurement devices, some preliminary tests are conducted with two cases (Case 1 and 2) that were repeated several times. In Case 1 and 2, coolant volumetric flow and temperature difference between coolant inlet and room are the same (0.05 l/s and 55 °C) but with different fan rotations (1000 rpm for Case 1 and 1500 rpm for Case 2). These rotational rates result in 1.59 m/s and 2.45 m/s average air velocity from hot wire probes which are comparable to air velocity that hoses in the under-hood are subjected to. During the first experiment, a turbine flowmeter was used due to availability issues instead of the magnet flowmeter which has lower accuracy than magnet flowmeter (uncertainty of 0.2% and 0.03% respectively). The comparing factor for this experiment is the difference of coolant's inlet and outlet temperature. The results according to Figure 3.11 are relatively close in two runs of the test for Case 1 and 2 but still too unstable.

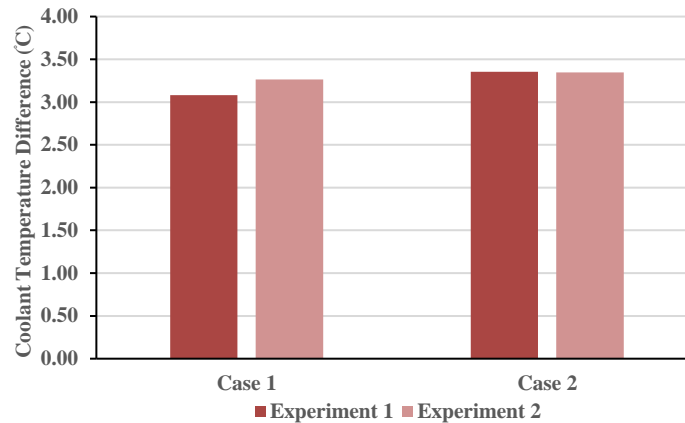


Figure 3.11 Coolant temperature difference comparison between experiment 1 and 2

These results shows that some modifications need to be done in the experiment measuring system to improve the measurement accuracy. Main factors which affect coolant temperature difference directly and are adjusted in each case are coolant inlet temperature, air fan rotation rate and coolant volumetric flow. The Coolant inlet temperature is adjusted by coolant heater controller and is measured by PT100s at coolant inlet. The fan rotation rate is controlled by a PWM controller and coolant volumetric flow is controlled by pipe and bypass valves and is measured by turbine flowmeter. Since the magnet flowmeter has higher accuracy in measuring flow rate, a new magnet flow meter was also installed in the circuit just before the coolant pipe.

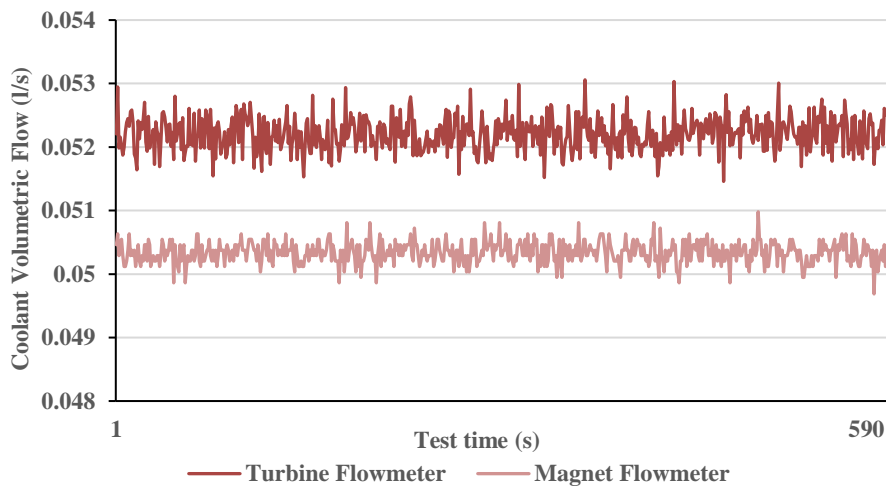
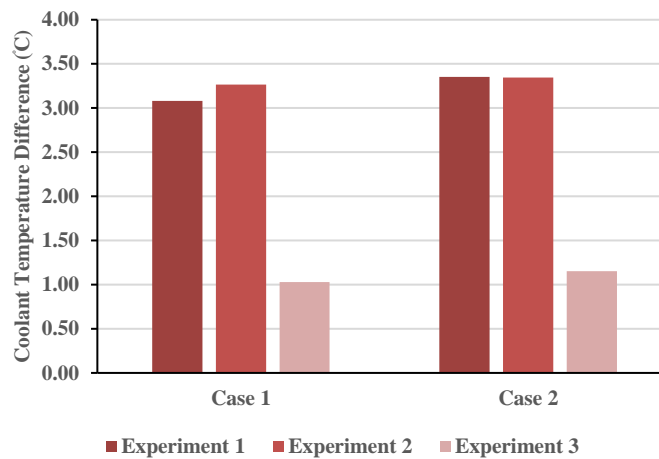


Figure 3.12 Comparison between turbine and magnetic flow meter measurement results in case 1

Figure 3.12 shows the comparison of turbine flowmeter and magnetic flowmeter in the same experiment for case 2 where the coolant flowmeter is set based on the magnetic flowmeter. It can be seen that the turbine flowmeter shows around 0.002 l/s higher volume flow than magnet flowmeter. Since the flow rate is one of the main factors in equation (6.2), small changes in this value can affect the temperature difference significantly. It can also be seen that the fluctuations in magnet flowmeter is lower than turbine flowmeter which can be helpful in reducing the uncertainty of the results. In

Figure 3.13 the results of the third experiment after installation of magnet flow meter can be seen.



*Figure 3.13 Coolant temperature difference comparison between experiment 1 to 3*

Figure 3.13 shows a sharp reduction in coolant temperature difference. This change can be due to the change of flowmeter to magnet flowmeter. Another reason can be the reduction of air in the coolant circuit according to the large number of conducting tests, since air in the circuit can make it harder to capture the real temperature difference based on different flow properties.

Considering the fan rotation rate according to the results we can see that the difference between case 1 and 2 is quite low when the rotation rate is changed from 1000 rpm to 1500 rpm. This can show that coolant temperature difference dependability on ambient flow velocity resulting from fan rotation is much less than on coolant flow rate. Hence no modification is done on the fan rotation rate measurement.

PT100s in coolant's inlet and outlet are the next main factor. These sensors were checked for calibration again and the results were within the acceptable range. Afterwards some correction coefficients are also mentioned in the calibration report of each PT100 which should be added to the measurement system. By adding these factors, the shown temperature is corrected by the deviation of the sensor. After adding these factors, the PT100s became more aligned in each side as can be seen in Figure 3.14.

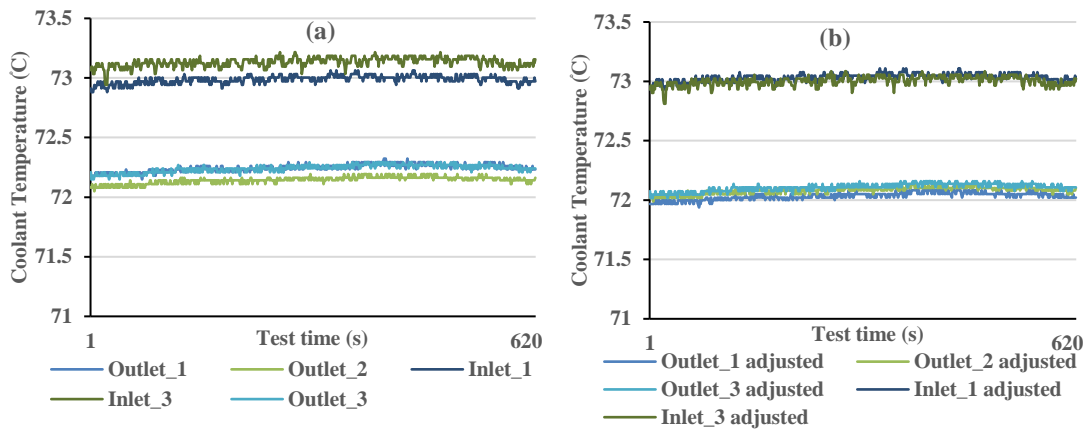


Figure 3.14 Temperature results of case 1 from thermocouples in coolant pipe's inlet and outlet (a) before and (b) after correction

The data in Figure 3.14 are from the same test of Case 1. As can be seen in Figure 3.13(a), before adding correction factors the signals were not aligned and some sensors' results were neglected if they were showing very off temperatures. By doing this, in fact some parts of data would be lost. After adding the correction factors, temperature results are quite aligned and reliable. By averaging over the corrected values, we improve the quality of the results.

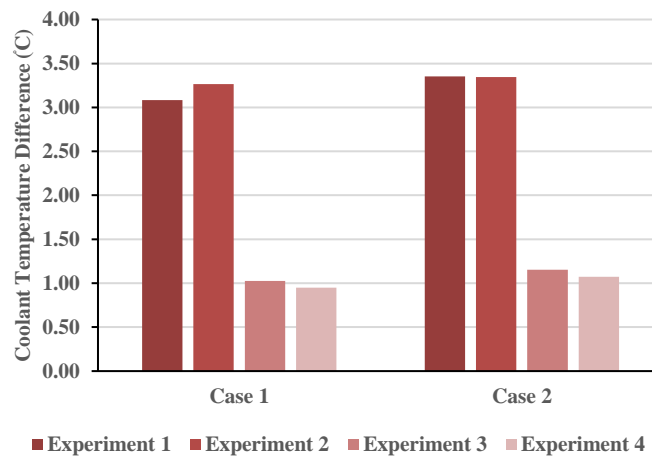


Figure 3.15 Coolant temperature difference comparison between experiment 1 to 4

The results in Figure 3.15 show small reduction of coolant temperature difference from experiment 3 to experiment 4. This reduction was expected due to Figure 3.14. From the results we can see that effect of flowmeter is more significant than the effect of PT100s' correction factors. From these results it can be claimed that experiment 4 has the most accurate results and this experiment's measurement system will be used for other cases as well. But we should also make sure that this experiment is repeatable. In the next section, the repeatability tests are explained.

### 3.1.7 Repeatability

Four cases were chosen for the repeatability test: Case 1, 2, 7 and 8. Case 1 and 2 are in the same coolant volumetric flow and temperature difference between coolant inlet and room (0.05 l/s and 55 °C) but in different fan rotations (1000 rpm for case 1 and 1500 rpm for case 2). In case 7 and 8 have also 55 °C temperature difference between coolant inlet and room in both and 1000 rpm for and 1500 rpm fan rotation rate for case 7 and 8, respectively. But they have lower volumetric flow rate (0.01 l/s) than case 1 and 2. The test was repeated for each of the cases five times in different days. Coolant temperature difference between inlet and outlet is used for comparison of the tests.

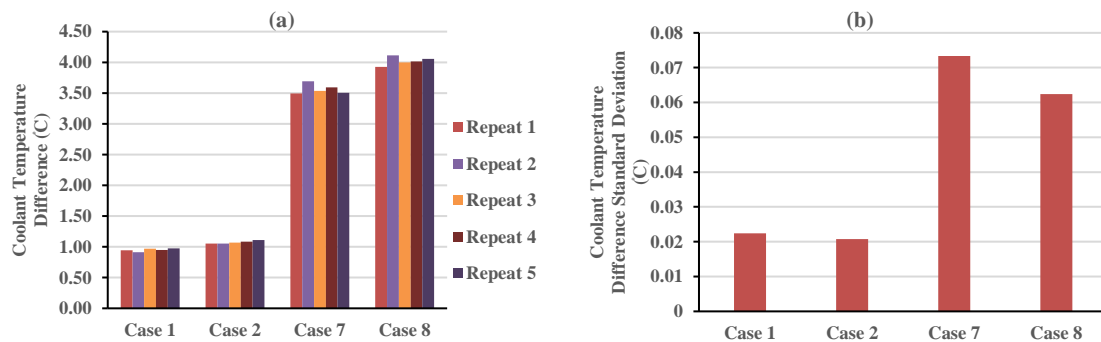


Figure 3.16 Repeatability test results in (a) coolant temperature difference comparison and (b) coolant temperature difference standard deviation between tests for each case

According to Figure 3.16, the temperature difference has remained the same in each case. The standard deviations are all below 0.1 °C which can be used in the uncertainty analysis of final tests. It can be seen that standard deviations of Case 7 and 8 are relatively higher than Case 1 and 2. The only difference between Case 1 and 2, and Case 7 and 8 is the coolant flow rate. Setting the coolant flow rate to 0.01 l/s (Case 7 and 8) compared to 0.05 l/s (Case 1 and 2) has the same human error but the difference in standard deviation shows coolant temperature drop is more sensitive to coolant flow rate in lower flow rates.

## 3.2 Computational fluid dynamics simulation

The second part of this study is trying to simulate the rig as close as possible to the experiment conditions. The rig is simulated in STARCCM+ CFD simulation software. The different modeling approaches and setting used for the simulation are explained in this part. It is also of interest how to simplify the simulation to get the same result or investigating the key factors which should be considered important in setting up the simulation or the factors which can be neglected. In the next section, two different models with different geometry considerations are proposed to show how important this factor is in the simulation.

### 3.2.1 Study of geometry scale

In CFD modeling studies, all the efforts are in the direction of simplifying the models to reduce the computational cost and time. Therefore, one of the focuses of this study is to investigate if a simplified geometry can be used for modeling instead to reduce the

computational effort/time needed to get the results. For this reason, two geometries are introduced to model the coolant's heat loss.

1. Simulating only the test section box without considering the fan. In this model box boundary conditions are set to velocity inlet and pressure outlet and average air velocity of two hot wire probes is considered for air velocity in the inlet. The geometry can be seen in Figure 3.17.



*Figure 3.17 Geometry modelled in box model*

2. Simulating the box considering fan and all the room where box is located. The room is not simulated based on the actual geometry of the test room but more to get the same air flow inside the box. In this model There is not any inlet and outlet flow into the room. The fan rotation is the only drive force for air flow. In Figure 3.18, the geometry can be seen.

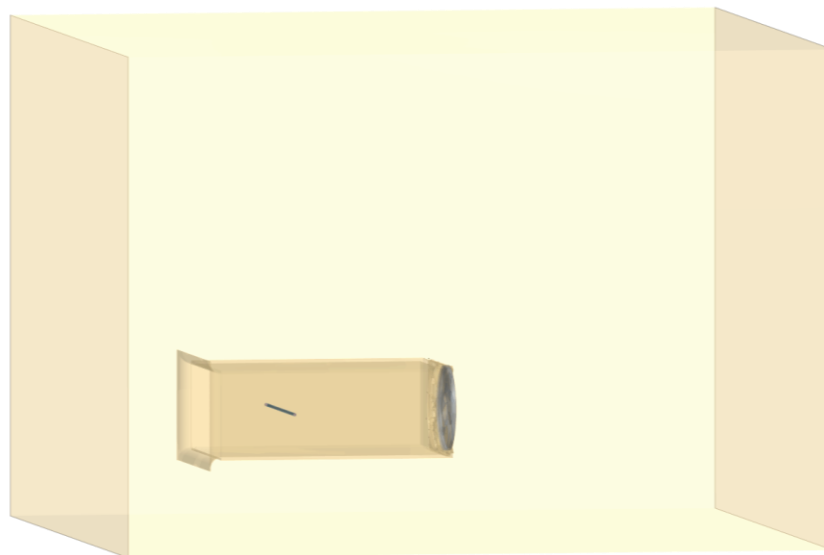


*Figure 3.18 Geometry modelled in room model*

Comparison of the results from these two models help us in understanding of the effect of flow field on the heat loss of the hose. In case where the results are quite similar, the simple model can be used instead of the room model.

### 3.2.2 Mesh for box model

In the box model, only box, pipe and coolant domains are meshed, with a Polyhedral mesher. The thin mesher is used to mesh the pipe and prism layers are used on the surfaces towards the air and the coolant side. Since the heat transfer phenomenon is simulated in this study, conformal mesh between domains of air, pipe and coolant is essential. These mesh features are precisely explained in the following sections.

#### 3.2.2.1 Thin mesher

A prismatic-style volume mesh can be created in thin sections of the geometry using the thin meshing approach. When compared to a comparable tetrahedral or polyhedral type core mesh, using this mesh decreases the cell count and improves overall cell quality. The convergence of simulations involving conjugate heat transfer in thin geometries can be improved using this kind of mesh. Regardless of whether the parts have a prismatic or polyhedral volume mesh, the thin mesher produces a conformal mesh between all concurrent parts that are included in the same Automated mesh operation. Thin plate geometries are the typical application for the Thin Mesher. High-quality cells are necessary in these geometries in order to accurately capture the thickness of the solid material. Then, any geometries in touch with one another can have heat transfer analysis done between them. Thin Mesher in this case is used in the pipe and can be seen in Figure 3.19.

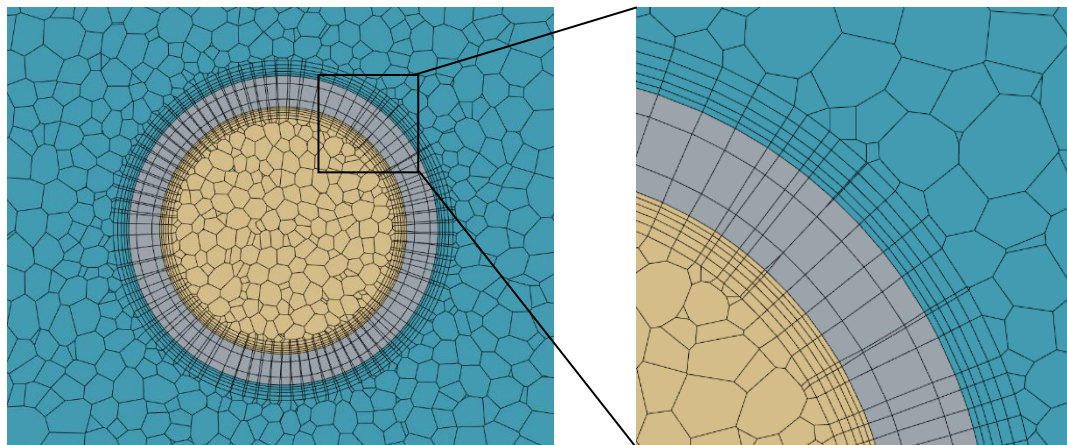


*Figure 3.19 Contact between coolant, pipe and air regions in mesh for box model*

#### 3.2.2.2 Prism layers

When paired with a core volume mesh, the prism layer mesh model creates orthogonal prismatic cells close to boundaries or wall surfaces. For the flow solution to become more reliable, this layer of cells is required. Prism layers give the solver the ability to precisely resolve near wall flow, which is essential for resolving boundary layer flows and identifying flow characteristics like separation in addition to forces and heat transfer on walls. Since the integral results like drag and pressure drop are impacted by separation, determining the velocity and temperature gradients normal to the wall is necessary for accurate prediction of these flow features. In the viscous sublayer of a turbulent boundary layer, these gradients are far sharper than what would be indicated by using gradients from a coarse mesh. If the turbulence model enables it, you can resolve the viscous sublayer directly by using a prism layer mesh. The thickness,

number of layers, and distribution of the prism layer mesh are determined by the chosen physics fidelity and the turbulence modeling methodology. In addition to offering near wall mesh density, prism layers enable the use of high aspect ratio cells, which improves cross-stream. Additionally, near the wall, prism layers reduce numerical diffusion. When the flow is in line with the mesh, numerical diffusion is minimized. In the case of this study for Box model, prism layers are used contact areas between pipe, and air and coolant region. They are also used in the box wall surfaces for resolving the flow separation more accurate but since these walls are quite far from the heat transfer area, which is close to the pipe, fewer number of layers are used for them to reduces the cost of simulation.

### **3.2.2.3 Conformal mesh**

A mesh with different geometric elements without breaking the mesh's continuity between contacting parts is called a conformal mesh [18]. The perimeter of coinciding cell faces on contacting parts and the cell faces on the surface of one part in a conformal mesh match exactly. Conformal mesh is highly recommended for conjugate heat transfer simulations where 2 or 3 different regions are in contact, and heat is transferred between them. In this experiment, the most important area for heat transfer is between pipe and air flow and pipe and coolant flow. Hence a conformal mesh is required in these areas. The conformal mesh can be seen perfectly in Figure 3.19 in the contact area between each region. In order to obtain the conformal mesh, regions must be imprinted on each other. Geometrically close surfaces or edges can be imprinted using the Imprint procedure, within a specified tolerance. When surfaces coincide, part contacts are formed between them.

### **3.2.2.4 Interfaces**

Interfaces are required in CFD simulation in order to be able to transfer solutions between two or three regions. Without an interface between regions, mass, energy, momentum or any other quantity cannot be transferred. In this study, a contact interface is used since this contact is used to connect two solid regions or a solid or a fluid region in which Conjugate heat transfer between the regions is allowed and according to this case is the best choice.

### **3.2.2.5 Mesh study**

One of the important steps to find the cost/time efficient simulation model is to find the mesh independent model. To achieve the lowest number of cells that still give accurate results, a mesh sensitivity analysis is done for the box model. Case 1 is used for simulation in this sensitivity study where volumetric flow rate of coolant is 0.05 l/s, temperature difference between coolant inlet and air is 55 °C and fan rotation rate is 1000 rpm.

Table 3.2 Mesh study for box model

Mesh	Cell count	Coolant Temperature Difference (C)	Maximum Y+ on outer Side of the pipe	Maximum Y+ on inner Side of the pipe	Surface averaged Y+ on outer side of the pipe
A	2743412	0,57	1.48	1.07	0.75
B	7895502	0,57	3.12	1.15	0.74
C	18348005	0,56	1.44	1.18	0.72

By changing from A to B, mesh is becoming finer in the pipe area and wake area and the mesh is finer in the air side in shifting form B to C. Despite the large changes in cell numbers, coolant temperature drop has not changed drastically, and all the results are in the same range. Near wall Y+ value is used to compare the meshes to understand how the flow resolution is especially near pipe. Maximum Y+ on the outer side of the pipe is highest for mesh B but considering the average value, it is within the range of other meshes and all of them fulfill the requirement of being below 1 (the average is close to 1). On the inner side of the pipe for all the meshes, the maximum Y+ values are within the same range close to 1 which again fulfill the requirement. It is clear that all the meshes in addition of showing the same coolant temperature difference, have enough resolution in the areas of heat transfer. For the reason of considering a higher resolution in pipe area as well as having less number of cells, mesh B is chosen for simulation. The detailed setup for mesh B can be seen in Table 3.3. The final mesh for box model can be seen in Figure 3.20.

Table 3.3 Specifications of mesh for box model

Air	base size	10 mm
	Target Surface size	5 mm
	Number of prism layers	3
	Prism layer thickness	5 mm
Air to pipe Surface	Target Surface size	0.75 mm
	Number of prism layers	5
	Prism layer thickness	1 mm
Wake refinement	Isotropic size	2 mm
Inner cylinder surface	Target Surface size	0.75 mm
	Number of prism layers	5
	Prism layer thickness	1 mm
Pipe surface	Target Surface size	0.5 mm
Inner cylinder	Base size	1 mm
Pipe	Base size	1 mm
	Number of thin layers	5

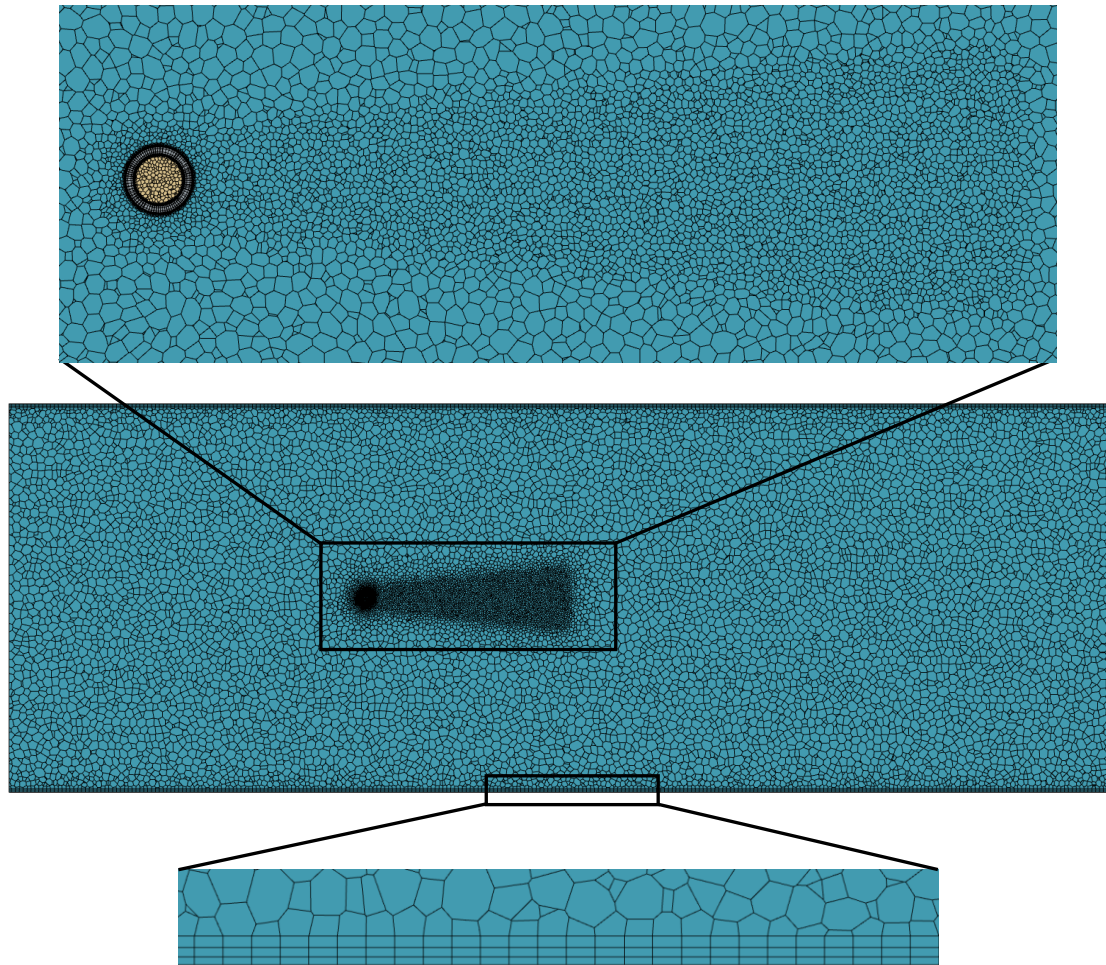


Figure 3.20 Mesh for box model

### 3.2.2.6 Study of coolant domain

In order to have a stable developed coolant flow in the pipe from the beginning of the box, the coolant domain was considered 5 cm longer than the box size from each side in the box model. Initially the plan was to have the same coolant domain in the room model, but this made problems in meshing of surface wrapper on the air side in case of intending to have conformal mesh. In conformal mesh it is needed to mesh all the parts together and this caused the two domains of air and coolant meshing the same part. To solve this problem, the coolant domain was reduced to the size of box's inner side. But to understand the effect of coolant domain length on the results, both cases were simulated in the box model and Coolant Temperature difference was compared between them. The simulation is done both for Case 1 and 18. The results can be seen in Table 3.4.

Table 3.4 Coolant domain comparison study

Coolant Domain	Air Model	Coolant Model	Coolant Temperature Difference (°C)	Difference between Short and Long Coolant Domain %
Short	k-epsilon	k-epsilon	0.57	0.24
long	k-epsilon	k-epsilon	0.57	

The results show a very small difference between Coolant domain models. Therefore, we can use the reduced coolant domain for the room model without expecting large error.

### 3.2.3 Room model mesh

Meshing the whole room model considering fan rotation is more challenging. Fan rotating area should be considered as a separate region with same physics continua as air region. The complex geometry of fan makes hard to mesh the air region. For this reason, surface wrapper is used to extract the volume for air region as well as for fan volume. In addition, simulating the complex conditions of the room and makes reaching to the promising mesh even harder. Choosing the boundary conditions for air in the room to reach the same air flow pattern inside the box is quite important in this level. Regardless of these modifications, the same settings in the box are used for the room mesh. Prism layer are also used between air and fan region but they are neglected in the room boundaries. Since the room was only added to model the fan flow and is not as much important as the box for heat transfer, larger cell sizes are used for room not close to the box. Final mesh for room model can be seen in Figure 3.21.

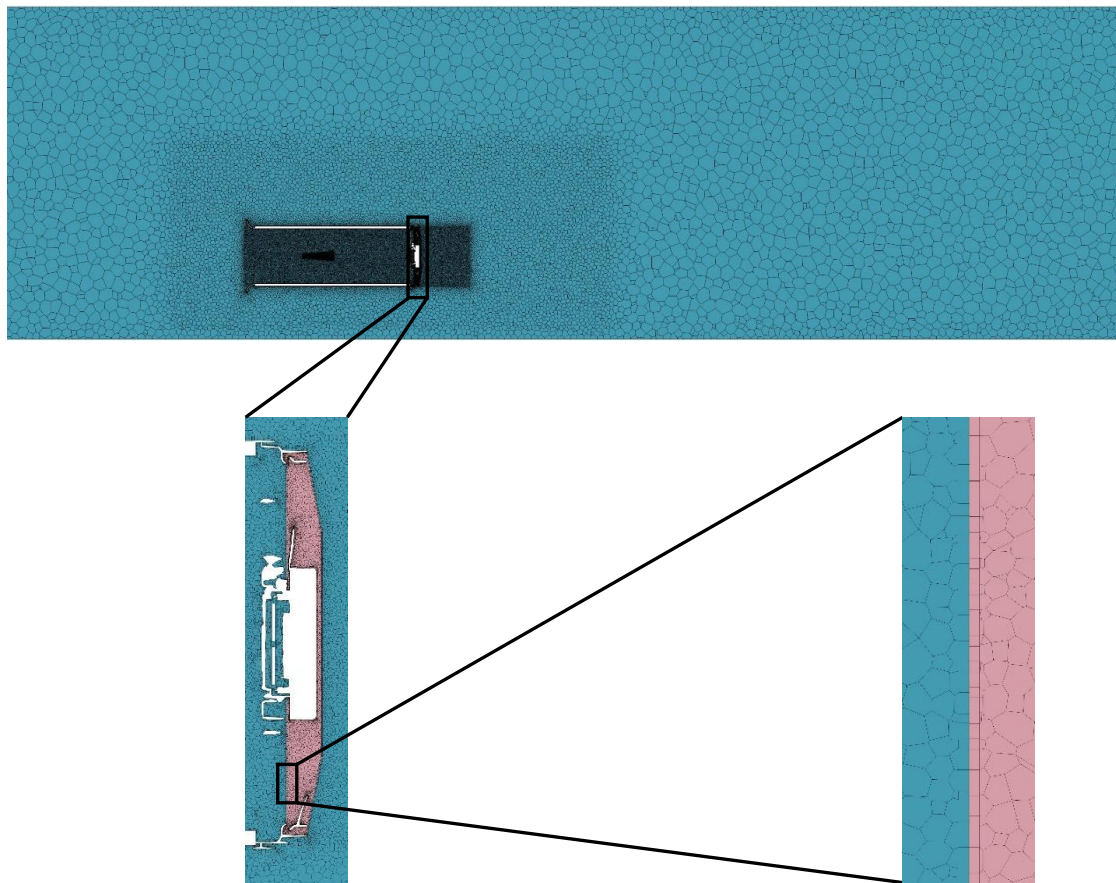


Figure 3.21 Mesh for room model

#### 3.2.3.1 Surface wrapper

When working with low-quality CAD data or complex geometries, the surface wrapper can be used to produce a manifold, closed, non-intersecting surface. Surface wrapper can be used in the geometries with for example mismatches in surface, several

intersecting parts, missing data being like gaps and holes and duplicate surfaces. Surface wrapper can solve all these problems by wrapping all the surfaces and simplifying the complex parts. Since the surface wrapper's output surface quality is not ideal, it is used with the surface remesher to give the volume meshers a high-quality beginning surface. To reduce the effect of poor-quality CAD data of fan geometry, surface wrapper is used for meshing air region as well as fan region.

### 3.2.3.2 Fan region

In order to simulate the rotation in the fan blades, a volume should be extracted approximately close to fan blades to conduct the rotation setting on it. This volume is created in ANSA and is designed to only include fan blades. The air outlet side is designed in a semi cone shape to prevent air flow in the perpendicular direction to the rotation axis. The fan region is extracted by surface wrapper between this volume and fan geometry which can be seen in Figure 3.22 and Figure 3.23. Rotation in the fan region can be modelled with two approaches of moving reference frame (MRF) and rigid body motion (RBM). These two approaches are explained in the following sections.

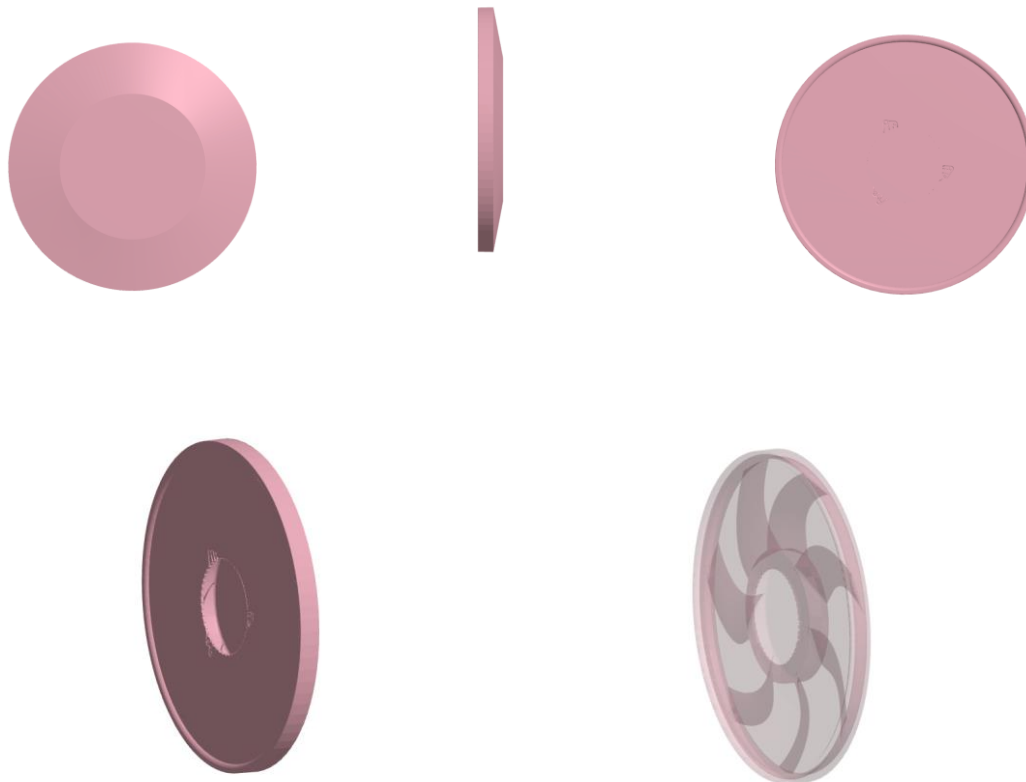


*Figure 3.22 Rotating part of the mesh in different viewpoints*



Figure 3.23 Left) fan geometry and right) fan geometry combined with fan rotating region

#### 3.2.3.2.1 Moving reference frame

A reference frame, which can be either stationary or rotating and translating with respect to it, is used to define mesh motion. Moving reference frames provide a method of representing rotations and translations as a steady-state issue while keeping the mesh constant in steady simulations or in transient simulations that do not necessitate a time-accurate solution. The location of cell vertices remains unchanged when an area is applied with a moving reference frame. Instead, in the associated conservation equations, it produces a continuous grid flux. The transient motion is transformed into a time-averaged solution using this modeling technique. Hence MRF is usually applied for steady state simulation. For the steady simulation part of this study, MRF is used for fan rotating part.

#### 3.2.3.2.2 Rigid body motion

In CFD, the position of a body can be changed with regard to the reference frame which can be described as motion. Mesh motion models in transient simulations let you move the computational domain's vertices through the simulation. It is possible to move the mesh rigidly in fluid mechanics applications by specified translations and rotations. For the transient simulations in this study, rigid body motion (RBM) model is used for fan region. Time step of the simulation is chosen to have a  $1^\circ$  rotation in each time step to ensure proper transport of the flow properties over the moving interfaces. This makes the simulation more time consuming but more accurate than MRF.

### 3.2.4 Models for steady and transient simulation

The test case of this study occurs in steady state. The measurements were conducted for long enough during the experiment (10 minutes) and the results were time averaged. Hence, steady-state simulations are expected to capture the same behavior just as well. The simulations should start from the least complicated models to optimize the simulation time. For the steady simulation, Reynolds averaged models (K epsilon Realizable and K omega SST) are used. In order to consider the effect of transient phenomena in the experiment as well and also prove the steady simulation results,

transient models are also used. For transient simulation, Detached Eddy Simulation (DES) which is a hybrid model which use both RANS and LES model is used.

### 3.2.5 Room model mesh analysis

The same settings from the chosen mesh of the box model are used in the room model's box area but the complexity of the room and its boundary conditions are important to consider as well in order to properly resolve the air flow which can affect the heat loss of the pipe. For this reason, a study is done on simulations with different room boundary conditions and the results are compared.

#### 3.2.5.1 Room boundary conditions analysis

Different meshes with different room boundary conditions are simulated for Case 1 with coolant volumetric flow of 0.05 l/s, 55 °C temperature difference between air and coolant inlet, and 1000 rpm fan rotation rate. In the first mesh, the room was simulated as a 3 m height, 4,2 m wide and 4,5 m long cube. The box was situated in the room showing in Figure 3.24. It is centered in y direction. The location is chosen to mimic the real room as best as possible. Other meshes are changed in relation to the first mesh. According to the room conditions for the experiment, for first mesh, room inlet was considered as wall and room outlet as pressure outlet. The steady simulation with k epsilon turbulence model for both air and coolant in Case 1 this mesh was ended in dverged solution.



Figure 3.24 Room sizing of mesh 1 for room model

This instability can be due to the high outlet flow from fan in the room outlet which causes instability in continuity equation. To solve this problem the distance between box and room outlet is increased from 2 m to 7.5 m. This can allow the fan flow to be resolved completely before reaching the room outlet. The simulation was again instable. To find the optimal simulation condition, different distances for inlet and outlet and different room boundary conditions are tried. The results of the study can be seen in Table 3.5.

Table 3.5 Mesh study for room different boundary conditions

Mesh	Number of Cells	Distance to Room Inlet (m)	Distance to Room Outlet (m)	Room Inlet Boundary Condition	Room Outlet Boundary Condition	Solution
Mesh 1	15694157	0.8	2	wall	pressure outlet	Diverged
Mesh 2	18011340	0.8	7.5	wall	pressure outlet	Diverged
Mesh 3	18109015	3	7.5	pressure outlet	pressure outlet	Diverged
Mesh 4	18264640	3	7.5	wall	wall	Converged
Mesh 5	18109015	3	7.5	pressure outlet	wall	Converged
Mesh 6	17963839	3	5.5	wall	pressure outlet	Converged

Pressure outlet is used as one of the room boundary conditions which is an outflow condition that defines the operating pressure [20]. According to the results, only the last three meshes succeeded in simulating the room model. Afterwards, we should decide on which mesh we should continue the simulations. The decision can be made based on the temperature pattern at the inlet of the box in the location of thermocouples, and the air speed pattern in the location of hot wire probes. For air temperature, there are 6 thermocouples at the inlet of the box. In order to compare the temperature patterns, temperature contour is drawn in the same plane as the thermocouples.

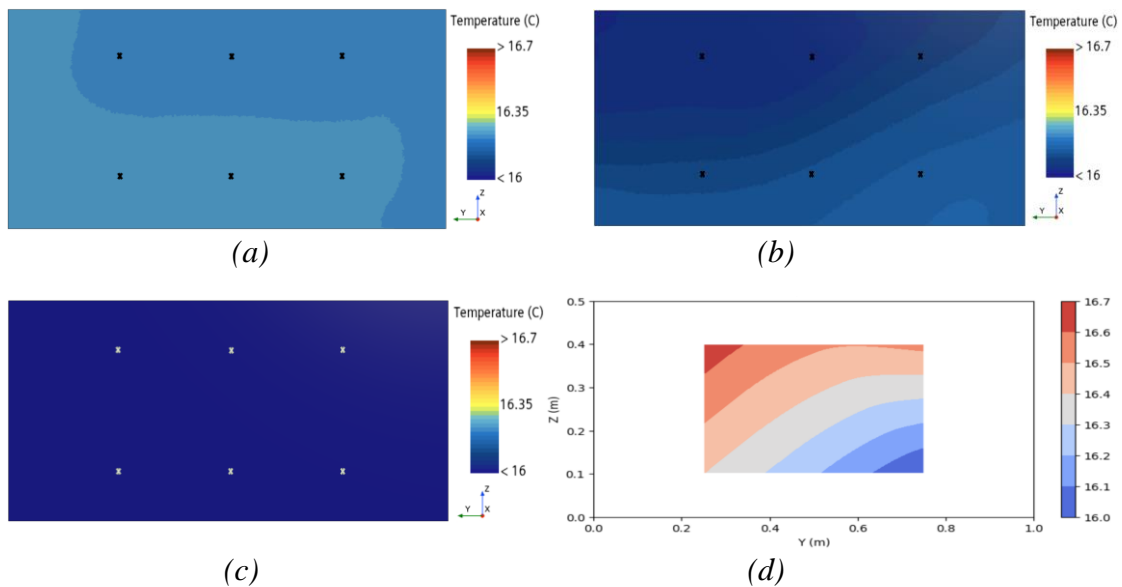


Figure 3.25 In picture a, b and c, temperature contours in the plane of the air temperature thermocouples for case 1 are shown for simulations with mesh 4, 5 and 6, respectively. The location of thermocouples are shown in temperature contours with black dots. d) Temperature contour drawn by the thermocouples' experimental data.

In Figure 3.25a, 3.25b and 3.25c, the temperature contours in the location of thermocouples for mesh 4, mesh 5 and mesh 6 simulation are shown, respectively. All the simulations are done in the same case with the same simulation model as described in Section 3.2.5.1. The location of each thermocouple is shown in the contours. In Figure 3.25c, the contour is drawn from the thermocouples captured temperatures in the same case's experiment test. Temperature profiles in simulations show an insignificant temperature gradient. Experiment data on the other hand show a large gradient between up and bottom temperature sensors around 0.7 °C. This difference is below the uncertainty of the thermocouples (1 °C) but still should be considered in comparison.

According to Figure 3.25a and Figure 3.25c, in the simulation with mesh 4 and 6 we barely have any temperature gradient and in the simulation with mesh 5 the temperature gradient is small and different compared to experimental data. Knowing the large uncertainty of the thermocouples, these experiment values cannot be reliable for comparison. Hence, air flow should also be compared between meshes.

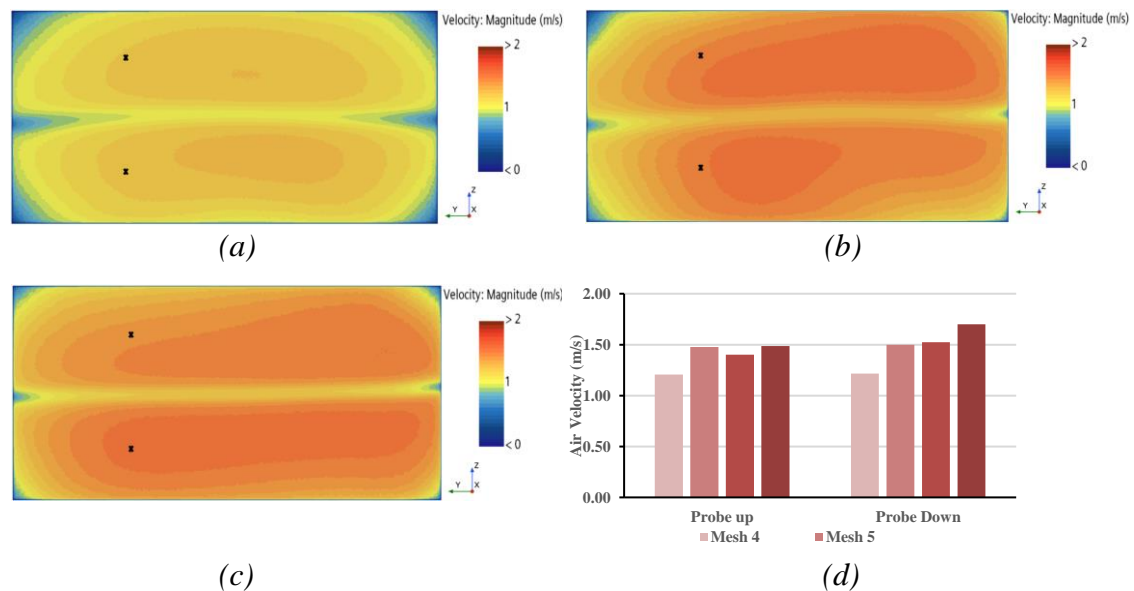
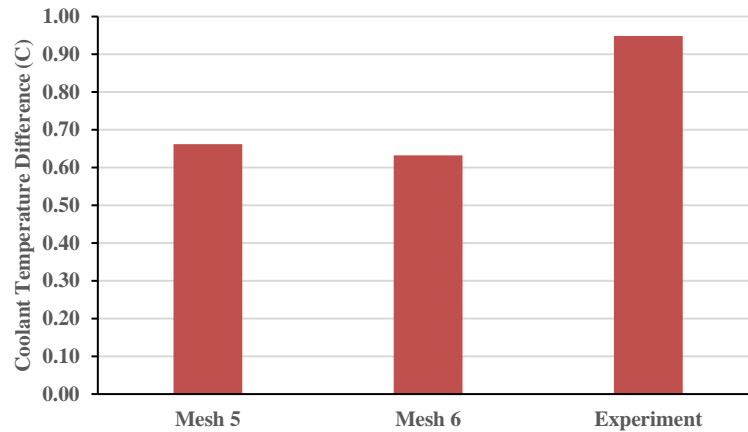


Figure 3.26 In picture a, b and c, air velocity contours in the plane of the hot wire probes for case 1 are shown for simulations with mesh 4, 5 and 6, respectively. The location of hot wire probes are shown in temperature contours with black dots. d) Comparison of air velocities in the hot wire probes with air velocities in the location of hot wire probes in simulations with mesh 4, 5 and 6.

The air velocity contours in the plane where hot wire probes are installed for mesh 4, 5 and 6 can be seen in Figure 3.26a, 3.26b and 3.26c, respectively. In Figure 3.26d, the velocity is of two hot wire probes in addition to the air velocity in the same location of the hot wire probes from the mesh simulations are compared. According to the results, it can be seen that mesh 4 has the lowest resemblance to the experiment with about 0.5 m/s difference with experiment results. This makes the simulation not realistic. By this it can be concluded that mesh 4 is not suitable for the simulation. Mesh 5 and 6 results are relatively close to the experimental results. In the experiment, the hot wire probe at the bottom shows higher air velocity than the top one. The same behavior can be seen in mesh 6. Mesh 5 also show the same pattern in the values in Figure 3.26d, but the

overall velocity pattern is in contrast. But the difference between top and bottom node in both two meshes is less significant than in the experiment. Furthermore, higher air velocity in the bottom hot wire probe cannot be expanded to the whole plane, since there are only two hot wire probes which are few to conclude the air flow pattern in the plane shown in Figure 3.26. Considering this, both mesh 5 and 6 can be regarded as suitable meshes for the simulation. In the next step, the coolant temperature difference between inlet and outlet can be compared to find the most accurate mesh.



*Figure 3.27 Comparison of coolant inlet and outlet temperature difference between meshes for room model*

The test case in this comparison is with the same simulation results for Case 1. According to Figure 3.27, mesh 5 and 6 show approximately the same value but the temperature difference in mesh 5 is closer to the experiment value. In this section by comparing the air temperature profile, air velocity profile and coolant temperature difference, the best mesh according to the room boundary conditions is chosen which is mesh 5 with room inlet as pressure outlet and room outlet as wall. This mesh has an acceptable box inlet air temperature pattern based on the temperature gradient, acceptable air velocity pattern and closer coolant temperature difference to the experiment than other meshes. But there is still a considerable difference between the simulation and experiment results regarding coolant temperature difference which is the focus of this study. For the next study, different turbulent models for both coolant and air side should be examined in both steady and transient simulations. Based on the similarities between mesh 5 and 6, mesh 6 should also be considered in simulation for comparison. In Figure 3.28, the air velocity field can be seen for mesh 5.

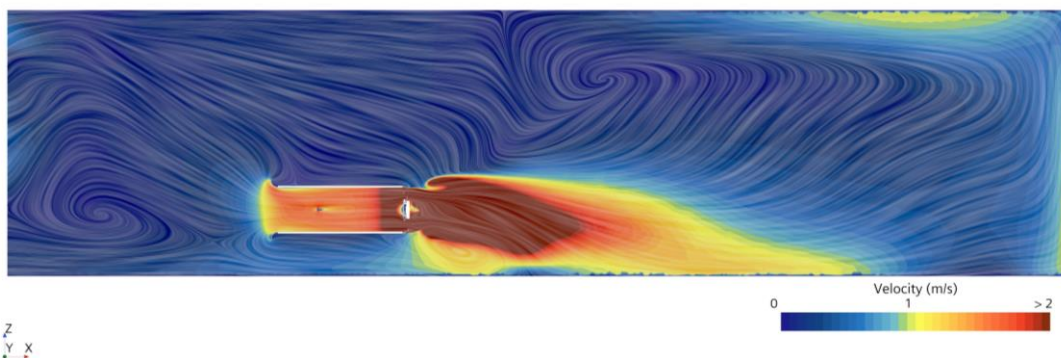


*Figure 3.28 Air velocity vector contour in the room model with mesh 5 for case 1*

### 3.2.6 Comparison of box model and room model

According to the geometry of the simulation, two model for geometry of the rig are introduced: box model in which only the box where the pipe is located is simulated, and room model in which the entire room of the experiment is simulated. By comparing these two models to the experiment results, we can understand their accuracy and decide to simplify the simulation to box model in case of high accuracy in this model.

The test case considered for comparison is case 1. This case is simulated with k epsilon turbulent model in steady simulation. In box model different inlet and outlet conditions are evaluated to see their effect on heat transfer and the stability of the simulation. The conditions can be seen in Table 3.6. Stagnation inlet boundary condition that is used for box inlet in box 2 model which is a condition usually used for compressible flows that in an imaginary space far upstream and the flow is at rest which can be used for incompressible flows as well [20]. The most important factor to compare is the temperature difference between coolant's pipe inlet and outlet. Initially, this factor should be compared in box models, room model and experiment. The comparison can be seen in Figure 3.29.

Table 3.6 Box models specifications

Model	Inlet Condition	Outlet Condition
Box 1	Velocity Inlet	Pressure Outlet
Box 2	Stagnation Inlet	Velocity Inlet with Negative Velocity
Box 3	2-part Velocity Inlet divided into Up and Down	Pressure Outlet

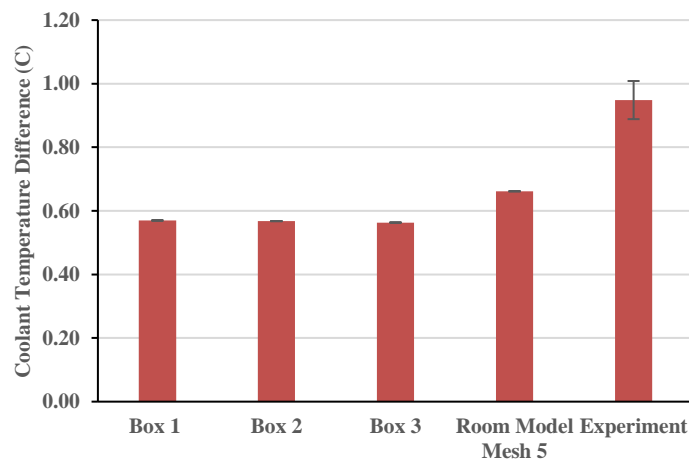


Figure 3.29 Comparison of box and room model

According to Figure 3.29, box models suggest a quite similar coolant temperature difference in all three models. We can make sure that the boundary condition does not affect the heat transfer in the pipe. As can be seen, coolant temperature difference in room model is closer to the coolant temperature difference in the experiment than in box models despite testing different boundary conditions. In order to understand the

difference between the room and box simulation, air velocity contour in the box can be compared between models.

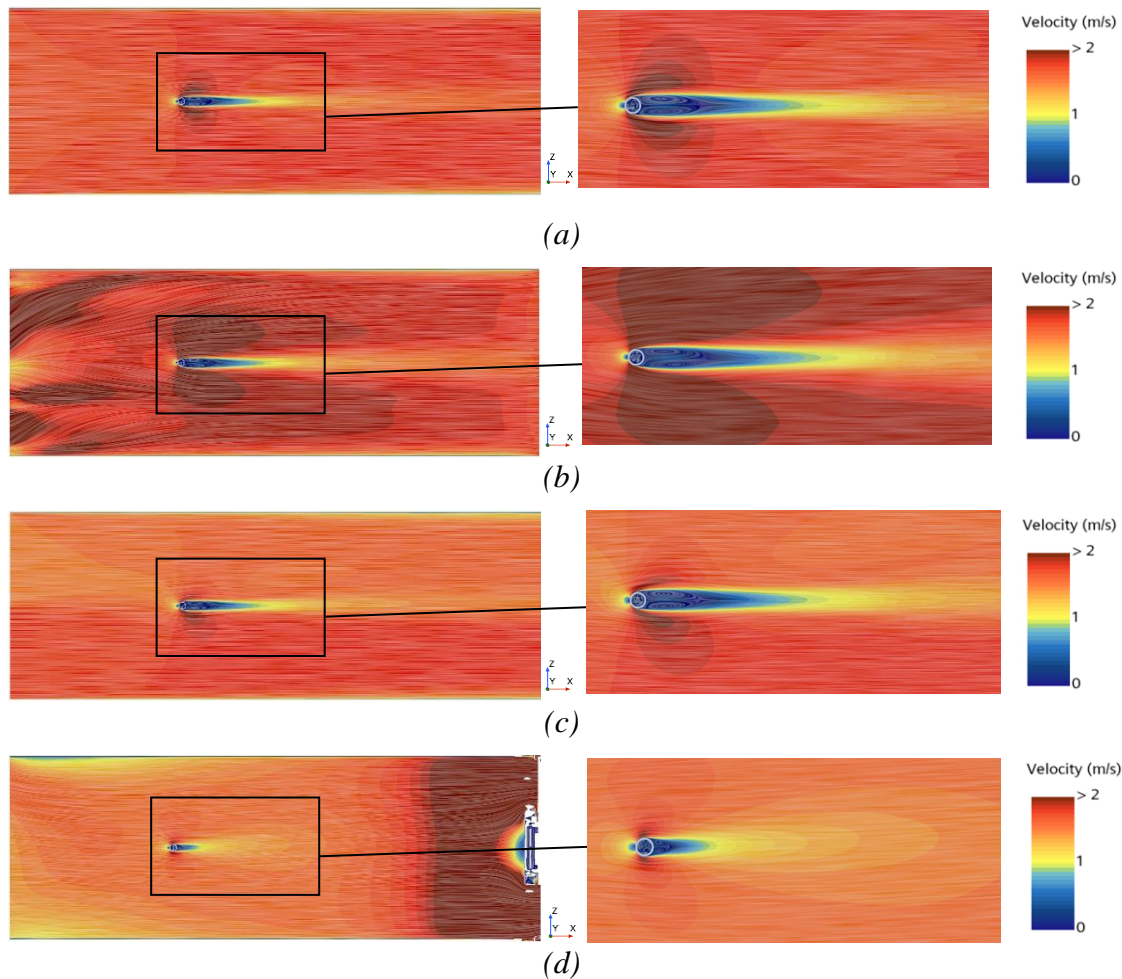


Figure 3.30 a, b, c, d) Air velocity contours for simulations with box 1, box 2, box 3 and room models, respectively.

Air velocity contours for box 1, box 2, box 3 and room model are shown in Figure 3.30a, 3.30a, 3.30c and 3.30d, respectively. In the box models, the time average of measured air velocities from hot wire probes is added to the inlet, and to the outlet as negative velocities in box 1 and 2 respectively. In box 3, the time average velocity of the top hot wire probe was added to the upper inlet section and average velocity of bottom hot wire probe in the lower inlet section. Based on this we can see that box models have different air flow patterns and different wake areas, but they all show higher velocities compared to the room model. This can be because hot wire probes are installed downstream of the pipe and having the same velocity in the inlet cannot produce the same air flow in the box. But this higher air velocity usually leads to higher heat transfer coefficient which leads higher heat transfer and coolant temperature difference. But in this case the higher velocity has led to lower coolant temperature difference. The reason can be seen in the wake area after the pipe. In the box models, the area with zero velocity involves a larger area on the pipe and is longer than in the room model. This change in wake area is caused on by the fan induced turbulence inside the box. This can reduce the total heat transfer in box models. For further investigation, the heat transfer contours on the pipe surface can be compared.

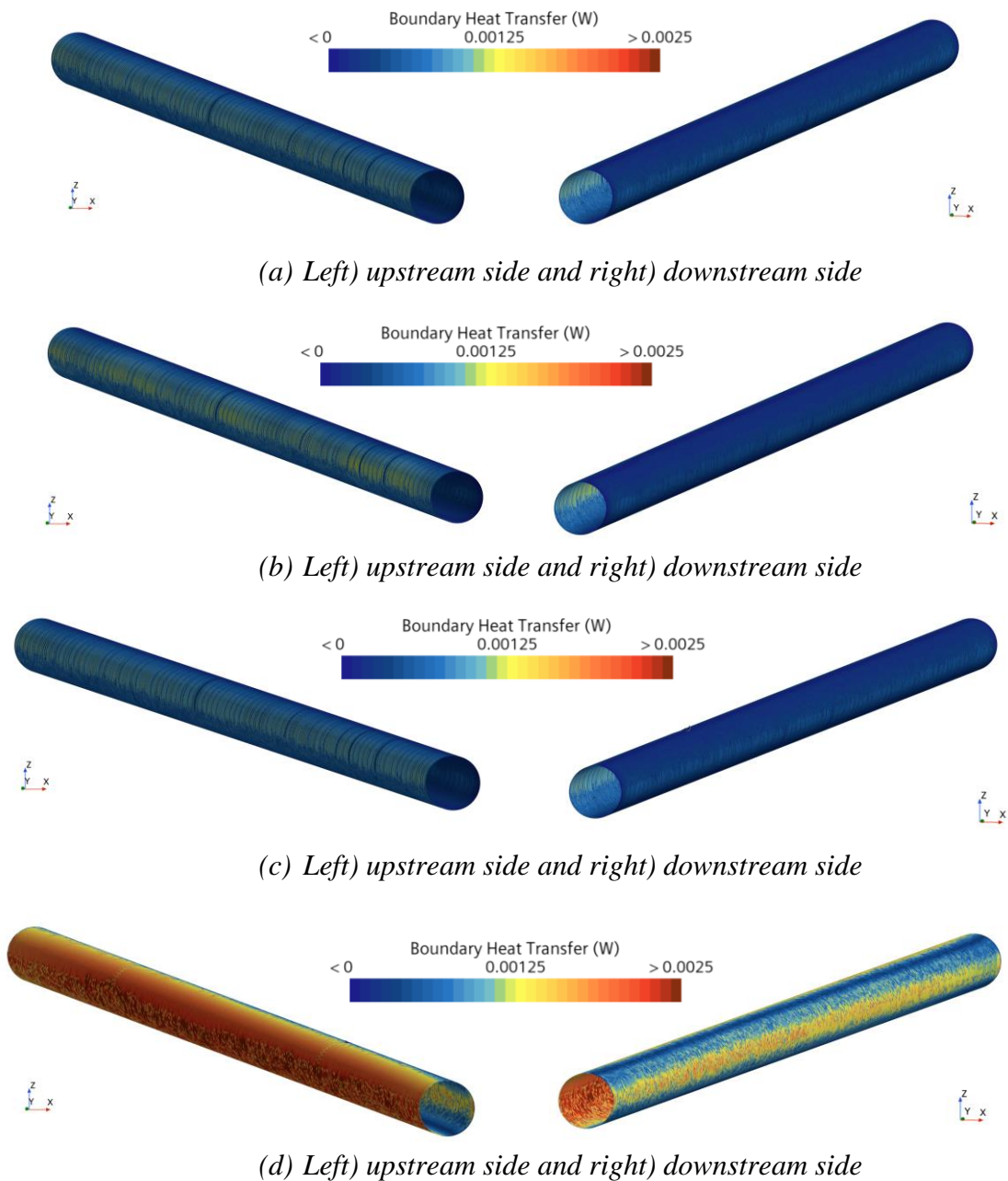


Figure 3.31 a, b, c, d) heat transfer on pipe surface in box 1, box 2, box 3 and room models, respectively

According to Figure 3.31, the heat transfer is clearly larger in room model than box models. Comparing to room model, heat transfer patterns in box models are relatively the same. A small rise can be seen in box 2 model which can be due to the changing in the box boundary conditions to have a suction flow other than blowing flow. This has changed the flow pattern and heat transfer slightly. Based on the opposite side of the pipe to air flow direction, we can see that the heat transfer in room model is even higher than the heat transfer in facing side of the pipe in box models. This shows that the flow circulation in wake area of the pipe in the room model is strong enough to increase the heat transfer rate. This phenomenon is induced by fan, and it cannot be neglected to the simulation of heat transfer.

Therefore, the simulation model cannot be simplified to the box model since it will neglect some of the heat transfer phenomena and it also has less accurate results than room model. The room model is used for the act of verification in the following sections.

### 3.2.7 Comparison of turbulence models on room model

In order to reach the most accurate simulation model to predict the heat loss of the coolant pipe, different turbulence models are investigated on room model mesh 5. In the steady simulation, for both coolant and air, models of RANS k epsilon and k omega SST are used. In steady simulation, MRF is used to model the fan rotation. For the transient simulation, RBM is used to simulate the fan rotation. DES turbulence model is used for air side in transient model and simulation results are for after 11 seconds. The results for each model simulating case 1 can be seen in Figure 3.33.

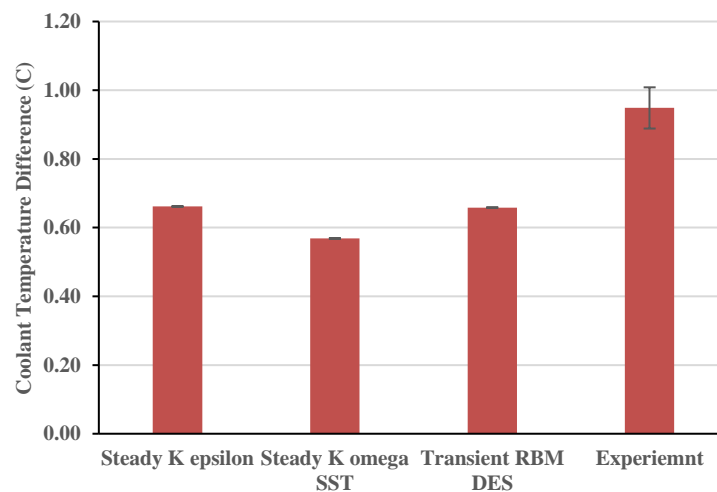


Figure 3.32 Model study on Case 1

According to Figure 3.32, using k omega SST turbulence model has not improved the simulations to show closer results to the experiment. It shows the same less accurate results as box models. Using the transient DES model does not show any changes from steady k epsilon model's results. The results should be investigated more in air flow patterns and heat transfer rates.

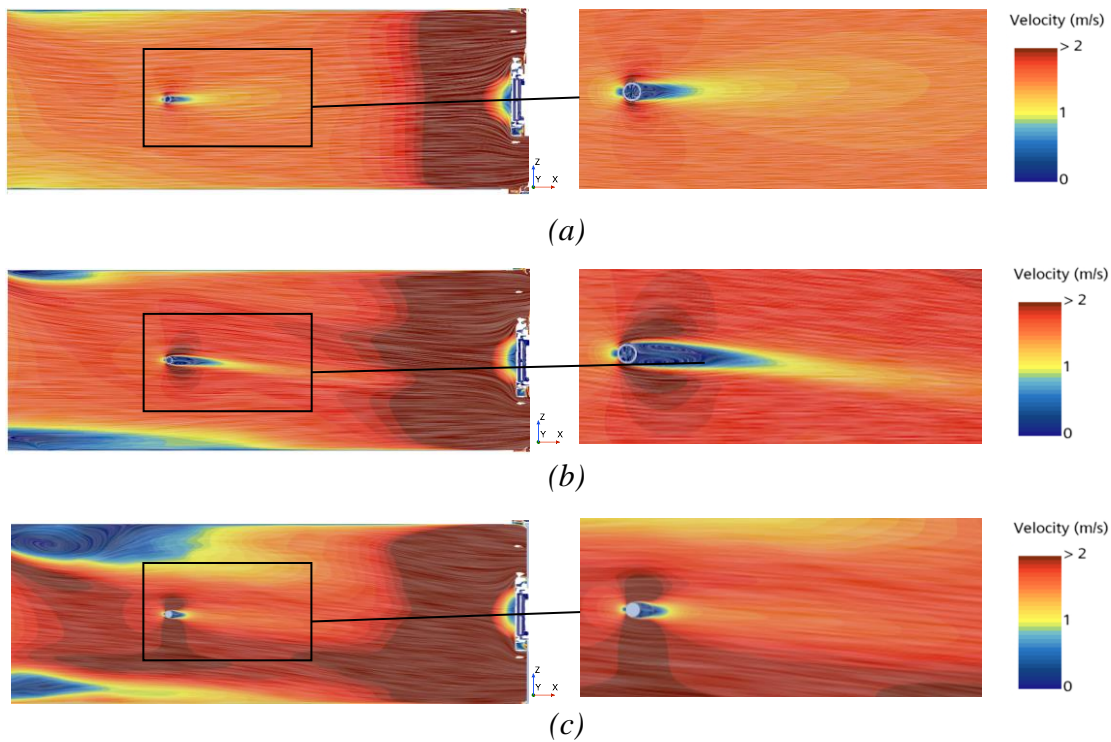


Figure 3.33 a, b, c) Air velocity contour for steady simulation with *k-epsilon* model, steady simulation with *k-omega* model and transient simulation with DES model, respectively

According to Figure 3.33, comparing with steady *k-epsilon* model, both steady *k-omega* and transient DES model show generally higher air velocity in the box. Comparing the pipe wake area, in steady *k-omega* model it is longer and involves larger share of the pipe surface resulting in lower surface with high heat transfer. This is due to the high accurate representation of *k-omega* model in boundary layer area which leads to more accurate turbulence resolution in wake area. In transient DES model, the turbulence flow is completely resolved in wake area. But the wake area resolved in DES model resembles the *k-epsilon* model more. The effect of this resolution in wake area should be seen in Figure 3.34.

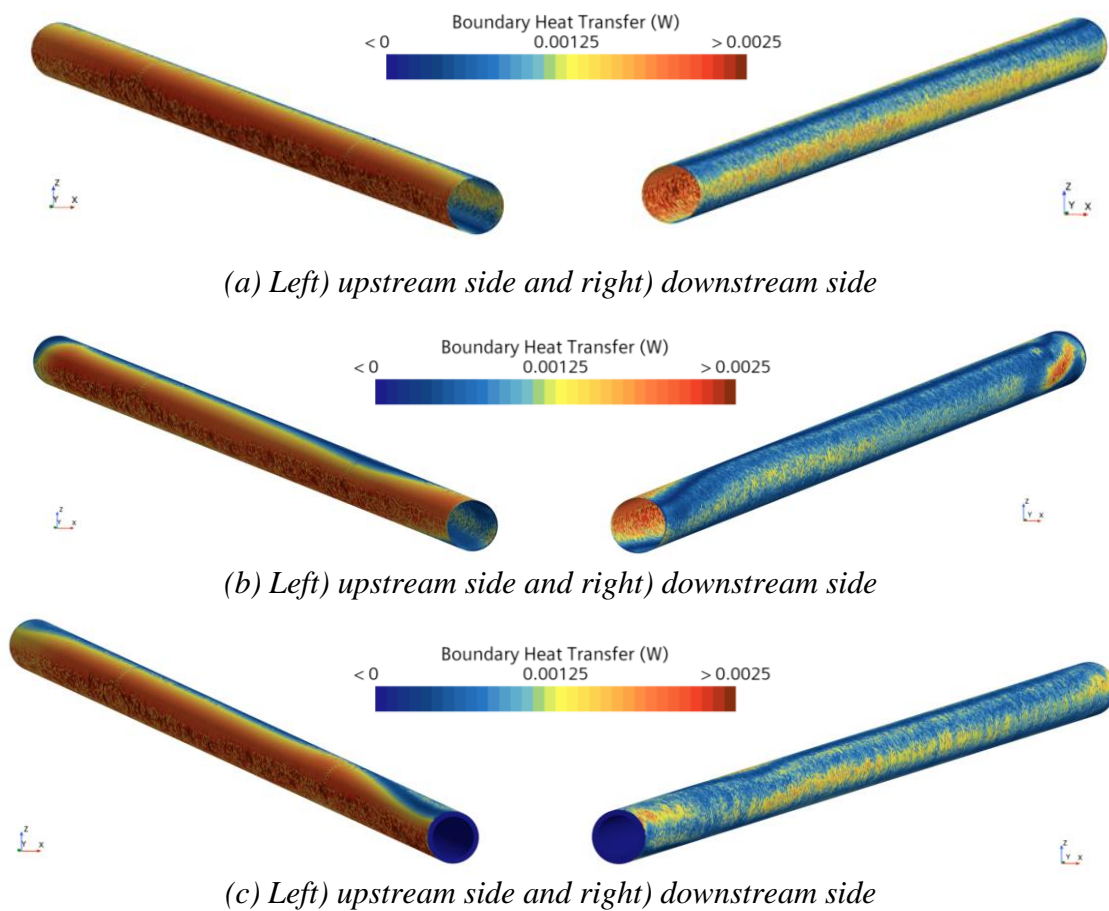


Figure 3.34 a, b, c) heat transfer on pipe surface in steady simulation with  $k$ -epsilon model, steady simulation with  $k$ -omega model and transient simulation with DES model, respectively

Based on Figure 3.34, as expected in steady  $k$ -omega model, the surface with high heat transfer rate is reduced. The heat transfer rate in the opposite side is considerably lower than steady  $k$ -epsilon model. This shows that the flow circulation in the wake area is not as strong as in steady  $k$ -epsilon model.

In the transient DES model, the heat transfer rate in the upstream-facing side of the pipe is approximately the same as for the steady  $k$ -epsilon model. In the downstream area of the pipe, the heat transfer rate have quite close pattern to the steady  $k$ -epsilon model. Generally, the heat transfer rate in transient DES model is similar to steady  $k$  epsilon model. This can also be seen in the results for coolant temperature difference. Hence, we can assume that there is no need to model the simulation in transient models with more accurate models since they will provide the same result eventually. According to this study of different turbulence models, based on the higher accuracy and cost efficiency, steady  $k$  epsilon model is chosen for simulation of other cases.

## 4 Results and discussion

In this section, according to decided meshes and optimal conditions for the experiment, achieved data from both experiment and simulation are shown, compared, and discussed. The experiment is conducted in order to measure the temperature difference in coolant's pipe inlet and outlet affected by air fan flow. The test cases are decided based on the cases described in Section 3. The experiment is also simulated in STARCCM+ by various models. The obtained results are shown in this section.

### 4.1 Comparison of coolant temperature difference

In this section, coolant temperature difference between inlet and outlet of the pipe is compared in experiments and the CFD simulations based on the chosen simulation settings obtained in Section 3. The results can be seen in Figure 4.1.

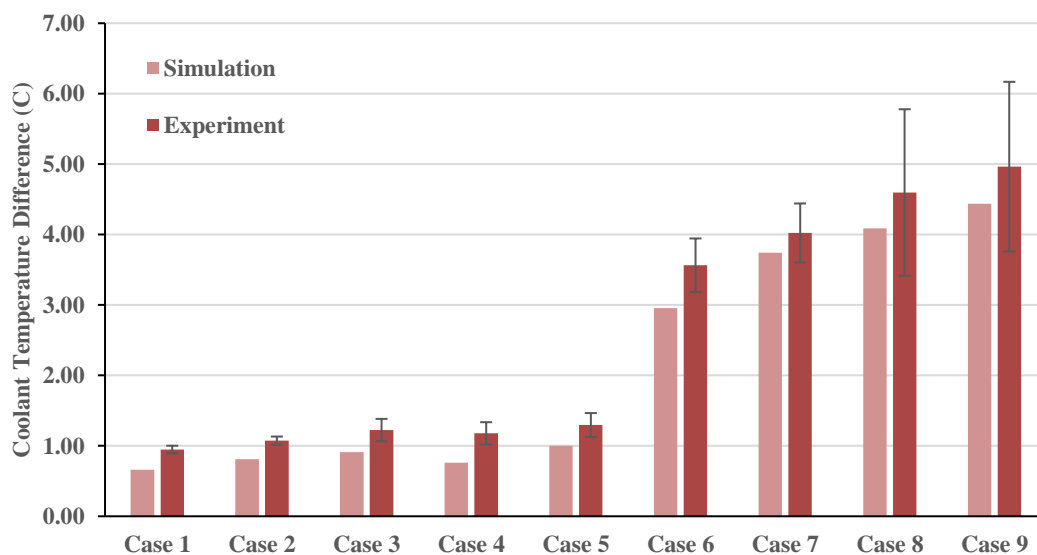


Figure 4.1 Comparison of coolant temperature difference in experiment and simulation. From Case 1 to 5, the coolant volumetric flow is 0.05 l/s and from Case 6 to 9, the coolant volumetric flow is 0.01 l/s.

The results of test cases are shown with their corresponding measurement uncertainty. The uncertainty is calculated by considering the uncertainties of all relevant measurement sensors (PT100s for coolant inlet and outlet, magnetic flowmeter for coolant flow, air velocity hot wire probes and air temperature thermocouples) [20, 21]. In case 1 to 5, the coolant volumetric flow is 0.05 l/s and is 0.01 l/s in case 6 to 9. For case 1, 2, 6 and 7 the uncertainty is updated by the repeatability test which have lower values relatively. It can be seen that the coolant temperature difference is increased drastically due to reduction in coolant volumetric flow. Comparing the test results with simulation results, it can be seen that the trend of change in both of them is the same. There is a slight difference between the test values and simulation values in each case. The difference is slightly increased with reducing the coolant's volumetric flow. In low volumetric flow rates, the simulation value stands in the uncertainty range of the test value, but it not the same on higher coolant flow rate cases. Overall, simulation values are lower than experiment values. The difference between experiment and simulation values are approximately in the order of accuracy of PT100s temperature difference

( $0.09 \times 2 = 0.018$  °C). And test and simulation were also done in the best possible conditions. Hence, we can consider the simulation model verified by the experimental data.

Therefore, the achieved data from both experiment and simulation should be investigated between cases to be able to understand the effect of each factor on coolant temperature difference.

#### 4.1.1 Impact of air velocity

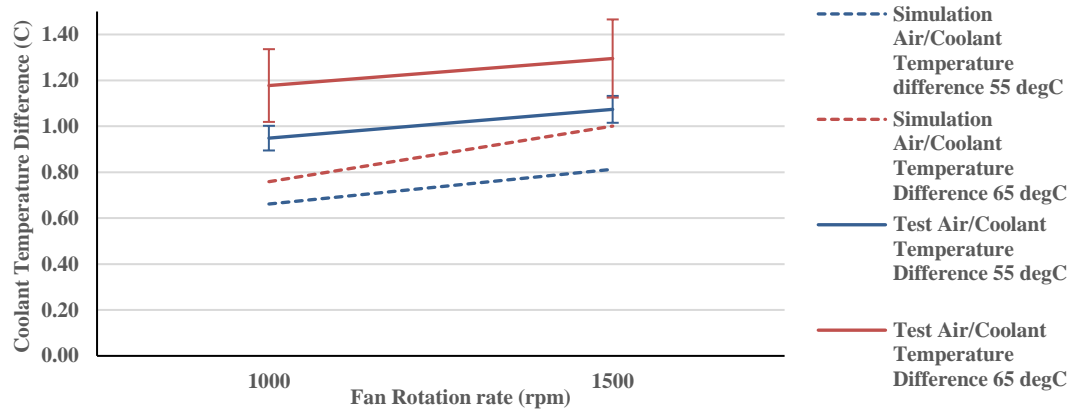


Figure 4.2 Effect of air velocity on coolant temperature difference in coolant volumetric flow of 0.05 l/s

In Figure 4.2, the effect of fan rotation rate on coolant temperature difference is investigated in different temperature differences between coolant inlet and air. The changes are shown between two fan rotation rates of 1000 rpm and 1500 rpm. Shifting from 1000 rpm to 1500 rpm rotation corresponds to approximately 1.69 m/s and 2.46 m/s air flow around the pipe respectively. As expected, temperature difference has increased with higher fan rotation rate/wind speed in both air/coolant temperature differences in both simulation and experiment. But this increase considering the change of fan rotation from 1000 rpm to 1500 rpm, is quite small. This increase can be explained by equation (4.1) extracted by equation (2.6) and (2.21) considering air temperature ( $T_{air}$ ) as constant and  $\bar{h}$  as total average heat transfer coefficient between air and coolant.

$$\Delta T_{coolant} = T_{coolant_{in}} - T_{coolant_{out}} = (T_{coolant_{in}} - T_{air}) \left( 1 - e^{-\frac{\bar{h}A}{mc_p}} \right) \quad (4.1)$$

By increasing the air velocity, overall heat transfer coefficient will increase and according to the equation, consequently coolant temperature difference will increase as it is verified in the test. But the changes in the heat transfer coefficient in the nominator of  $\left(-\frac{\bar{h}A}{mc_p}\right)$  will make small contribution to the changes in  $\left(1 - e^{-\frac{\bar{h}A}{mc_p}}\right)$  which is why the effect of the fan rotation rate is not that significant. By looking closely at Figure 4.2, it might come to mind that all the plots should have the same slope and the dashed red plot which is for the simulation of 65 °C air/coolant temperature difference, is the odd plot. But in contrary with comparing this plot and the dashed blue plot which is for the simulation of 55 °C air/coolant temperature difference, the slope of the dashed red plot is higher than the dashed blue one. By investigating equation (4.1), we can see that the

changes in coolant temperature difference affected air velocity is always scaled by the factor of  $(T_{coolant_{in}} - T_{air})$ . Therefore, the plot with higher  $(T_{coolant_{in}} - T_{air})$  should have higher slope which perfectly aligns with two simulation plots. Considering this fact, the odd plot will be the red plot which is the test data for the same cases as dash red plot. Expecting the same behavior, the red plot should have the same slope as dash red plot, but it does not. This can be explained by the uncertainty margins in Figure 4.2. Considering the margins for the uncertainty of the data, red plot can also have the same behavior as the dash red plot.

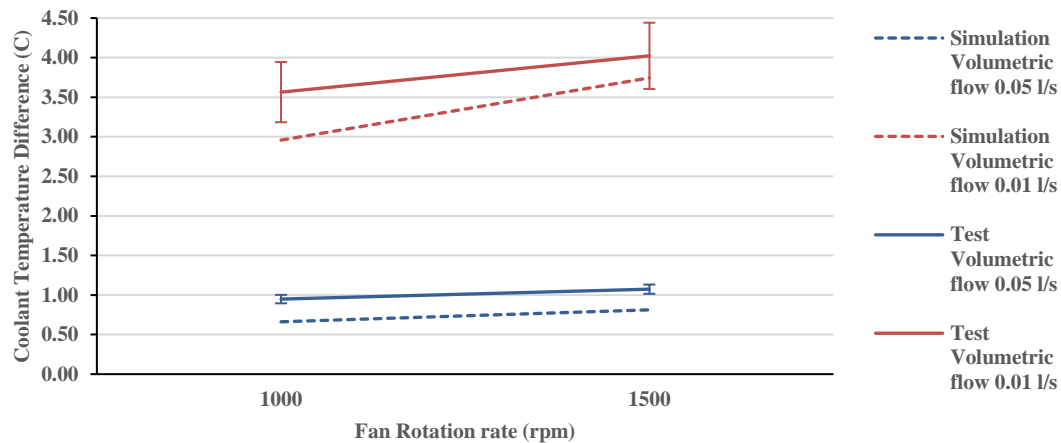


Figure 4.3 Effect of air velocity on coolant temperature difference in 55 °C temperature difference between coolant inlet and air

In Figure 4.3, the effect of fan rotation rate is examined in different volumetric flow. The same as Figure 4.2 with increase in fan rotation, coolant temperature difference has also increased in both coolant volumetric flows. It can be seen that with lower volumetric coolant flow, the slope of the lines is steeper. This is reasonable since when the mass flow rate reduces, the coolant flow will be more affected by changes in air velocity. This can also be proved in equation (4.1). According to this, we understand that the odd plot is the red plot which is the experiment for 0.05 l/s coolant flow. The slope of this plot is expected to be the same as the simulation of this case (dash red plot). We can also see that the difference between plot of 0.01 l/s and 0.05 l/s is considerable. Hence the effect of volumetric flow should also be studied.

### 4.1.2 Impact of coolant flow

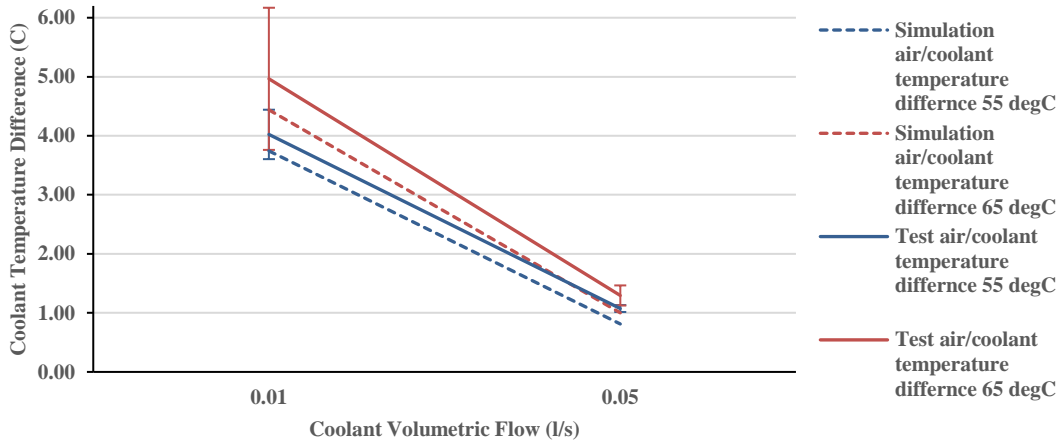


Figure 4.4 Effect of coolant volumetric flow on coolant temperature difference in fan rotation rate of 1500 rpm

According to Figure 4.4, coolant volumetric flow drastically affects the coolant temperature difference. By reducing the coolant flow from 0.05 l/s to 0.01 l/s, coolant temperature rises around 3 °C for all air/coolant temperature differences. According to equation (4.1), by reducing the coolant flow,  $\left(1 - e^{-\frac{\bar{h}A}{mc_p}}\right)$  will increase and this will increase the coolant temperature difference. The difference between plots with difference air/coolant temperature differences is rather small. This shows that the effect of volumetric flow is more dominant than other factors, like the air velocity. The behavior of each simulation and test plot of the same air /coolant temperature difference is the same and with increase in air /coolant temperature difference the slope of the plots is increased. This change was explained in Section 4.1.1.

### 4.1.3 Impact of coolant temperature

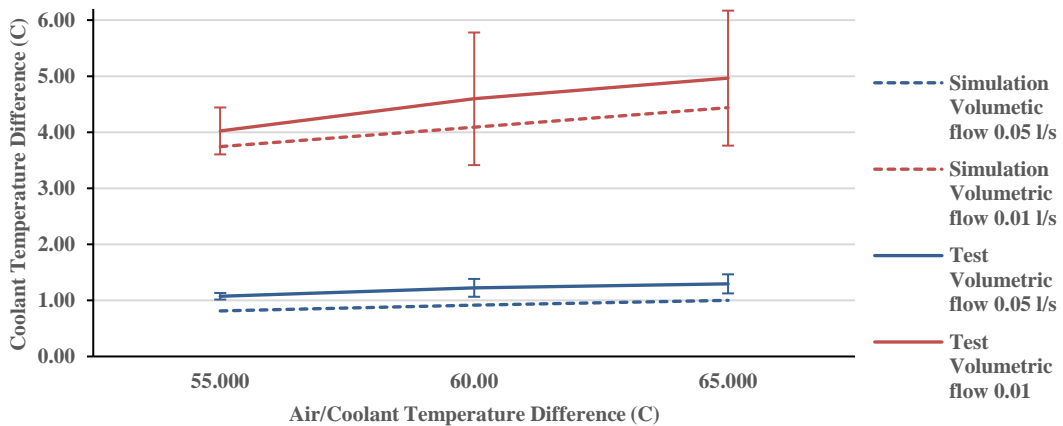


Figure 4.5 Effect of temperature difference between coolant pipe unlet and air with fan rotation of 1500 rpm

According to the Figure 4.5, the coolant temperature difference has increased with increase in this factor, but the changes are rather small. For explanation from equation (4.1), with large changes in  $(T_{coolant_{in}} - T_{air})$  since the it is multiplied by a small factor of  $\left(1 - e^{-\frac{hA}{mc_p}}\right)$ , the final coolant temperature difference will not be much increased. It can also be seen that with higher coolant flow rate, the changes in coolant temperature difference are larger which is previously explained.

By investigating these graphs, we understood that among the examined factors, coolant flow rate influences the coolant temperature difference the most. It also shows that the temperature drop in coolant is slightly affected by air flow and air temperature. These results can be helpful in studies of heat loss reductions in coolant hoses.

## 4.2 Comparison of heat transfer coefficient

One of the main focuses of this study is to provide a model to predict the heat transfer coefficient of coolant pipes correctly. For this reason, the calculated overall heat transfer coefficient between coolant and air from experiment is compared with predicted value in CFD simulations in this section. The results can be seen in Figure 4.6.

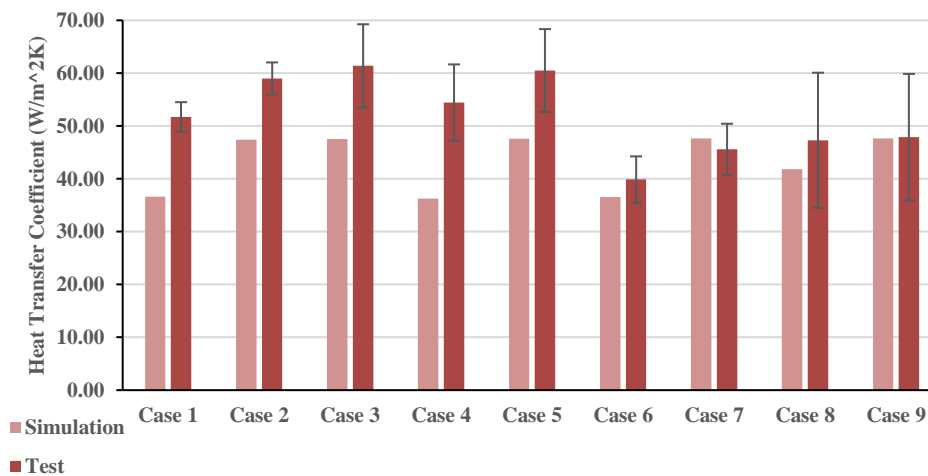


Figure 4.6 Comparison of overall heat transfer coefficient in experiment and simulation. Form Case 1 to 5, the coolant volumetric flow is 0.05 l/s and from Case 6 to 9, the coolant volumetric flow is 0.01 l/s.

In Figure 4.6, cases 1 to 5 have 0.05 l/s and cases 6 to 9 have 0.01 l/s for coolant volumetric flow. According to the results, for cases with higher coolant flow difference between experiment and simulation results are larger. Simulation results are slightly lower than the uncertainty range of the experiment results. In cases with lower coolant flow, the simulation and experiment results are reasonably well aligned. The different behavior of each case should be discussed further based on the settings of each case.

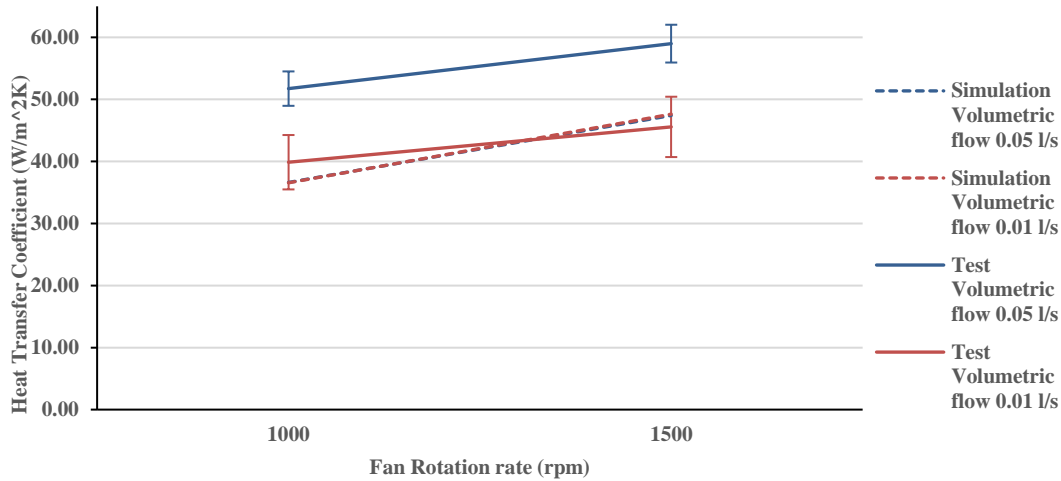


Figure 4.7 Effect of air velocity on overall heat transfer coefficient in 55 °C temperature difference between coolant inlet and air

As can be seen in Figure 4.7, the heat transfer coefficient is directly increased by the increase of fan rotation rate. But it can be seen that for the simulation results, the plots are quite the same regardless of the coolant flow rate. However it is increased in experimental results by increasing coolant flow rate. This aspect is further investigated in Figure 4.8.

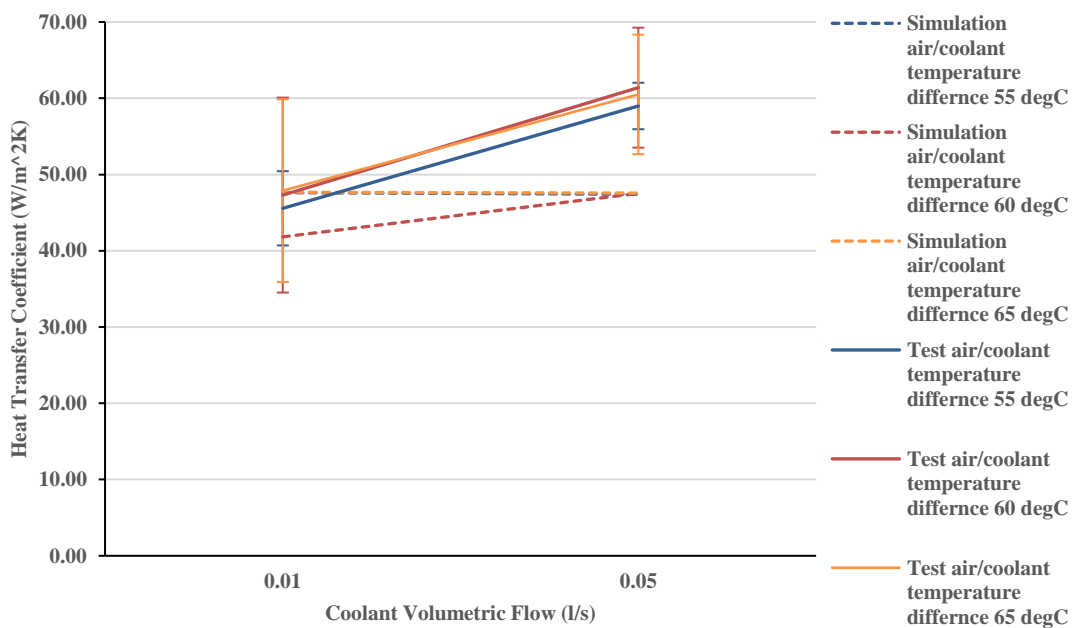


Figure 4.8 Effect of coolant volumetric flow on overall heat transfer coefficient in fan rotation rate of 1500 rpm

According to Figure 4.8, it can be seen that 2 out of 3 simulation plots (dash blue and dash yellow plot) are constant with changes in coolant flow rate and they are completely matching despite having different air/coolant temperature differences. Only one simulation plot (dash red plot) with air/coolant temperature difference of 60 °C shows rise in heat transfer coefficient by increasing the coolant flow rate. This show that the

heat transfer coefficients achieved from simulations are only affected by the increased air flow due to the higher fan rotation rate. This behavior can be explained by the getting deep into the calculation for obtaining overall heat transfer coefficient in a series of heat resistances. In a series where in this case is coolant flow, pipe and air flow, the material with lower heat transfer coefficient will be dominant and the overall HTC will be approximately in the same range of the lowest HTC which here air flow has the lowest HTC by distance from others. That is why the overall HTC is only controlled and affected by air velocity. These conclusions are only made based on simulation side and approved by empirical relations in analytical approach. The different observed behavior of experimental results can be explained by error bars which are large compared to the slope of the curves, making it uncertain if the experimental behavior is not similar to the simulations.

On the other hand in the experimental results, heat transfer coefficient is clearly affected by increase of coolant flow rate and is increased. But considering the uncertainty range for experimental data, they can also show a constant behavior. Two approaches can be used here to analyze the data: first, the behavior of HTC that is only affected by air velocity is the correct correlation and by considering the uncertainty range for experimental data, this correlation is approved by the experiment. In the second approach, the increase in all three experiments' plots shows that HTC is affected by coolant flow rate or other factors which are not considered in the simulation. Considering the second approach, further investigation should be done in this area to understand the affecting factors on HTCs.

In general, the predicted HTCs in cases with 0.01 l/s coolant volumetric flow, are in good match with experimental values. But in cases with 0.05 l/s coolant volumetric flow, the predicted HTCs are at most 25 % lower than the experimental values' lowest uncertainty range. The model has performed better predictions in lower coolant flow rates than higher. This correction factor can be used to modify the HTCs in higher flow rates in 1D simulations.

## **4.3 Additional simulations**

### **4.3.1 Upstream wall study**

After finding the best simulation setting for the test cases, it is intended to understand the effect of obstacles in the air stream on the heat transfer of the coolant pipe. Therefore, a 10 cm wall located 8 cm from the pipe upstream of it is added to the simulation. The study does not investigate the effect of wall in experiment since the results would have too large error margin to be comparable with simulation data. Instead, it is assumed that the simulation model is validated to be used on more complex geometries. This study can show how obstacles can change the air flow after the wall and how this change can affect the heat transfer. The turbulence model for this study is chosen the same as the most accurate model for test cases. The mesh for this study can be seen Figure 4.9.

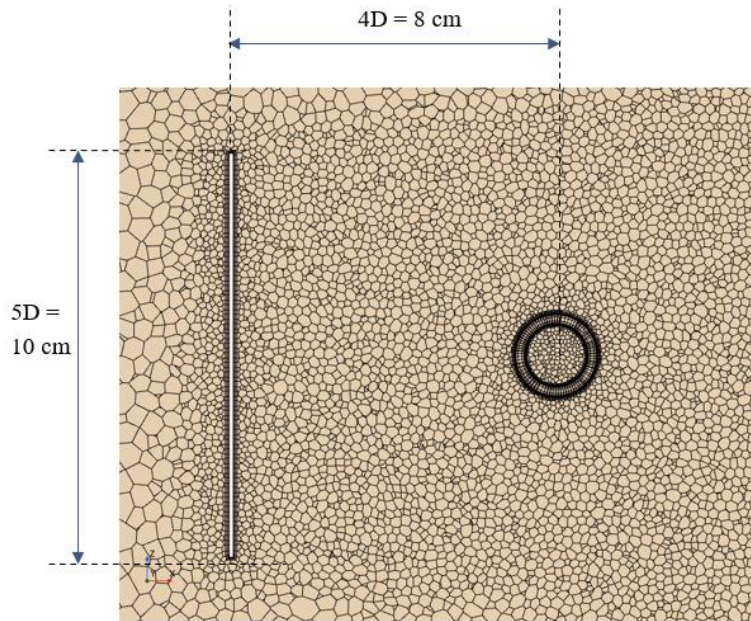


Figure 4.9 Geometry of wall added upstream of the pipe in mesh for room

Adding a wall upstream of the pipe is the next part of this study. This is added to understand the effect of barriers through the air flow on HTC of the coolant pipe. The effect of wall is simulated in case 1, 6 and 7. In Figure 4.10, the effect of upstream wall on coolant temperature difference in these cases can be seen. For all the cases adding the wall has resulted in reduction of coolant temperature drop by 50%. This effect can also be seen in HTCs which also have reduced in the order of 50% in all investigated cases. According to Figure 4.11, after adding the wall the plots of coolant temperature difference and HTC behavior in changing between cases have the same trend as before adding the wall. These behaviors should be investigated further in the air flow pattern and heat transfer coefficient on pipe surface.

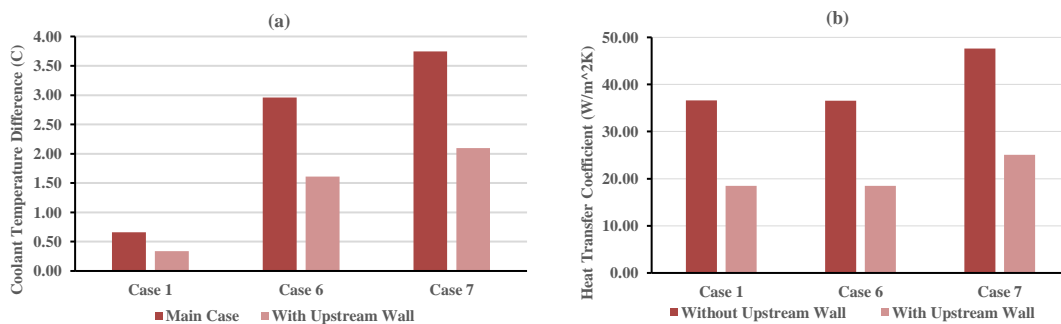


Figure 4.10 a) Comparison of coolant temperature difference between simulations of main cases and cases with upstream wall b) Comparison of overall heat transfer coefficient between simulations of main cases and cases with upstream wall

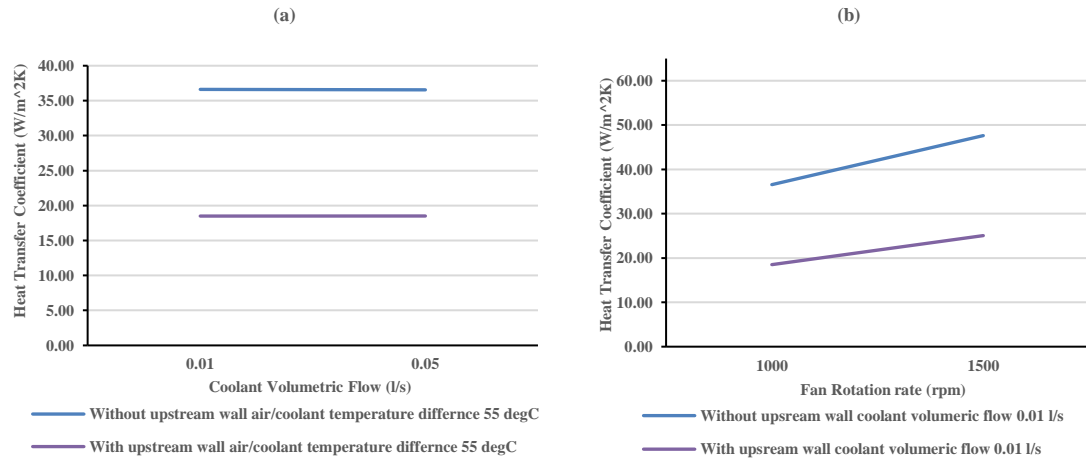


Figure 4.11 a) Comparison of effect of coolant volumetric flow on heat transfer coefficient between simulation results with and without upstream wall b) Comparison of effect of fan rotation rate on heat transfer coefficient between simulation results with and without upstream wall

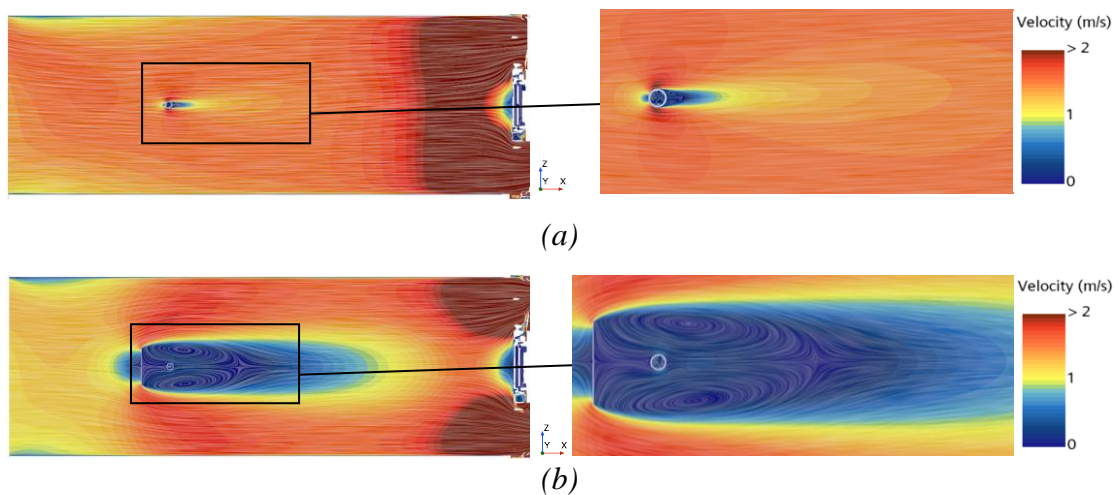
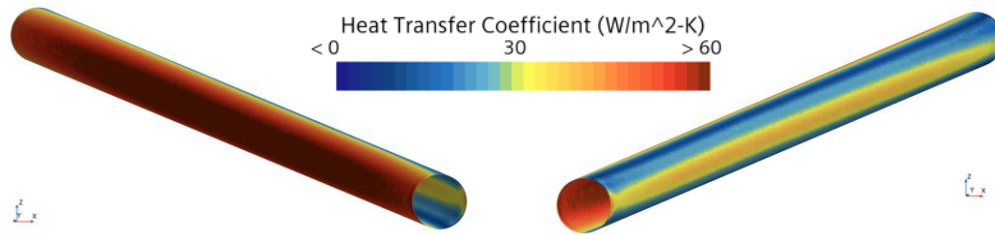
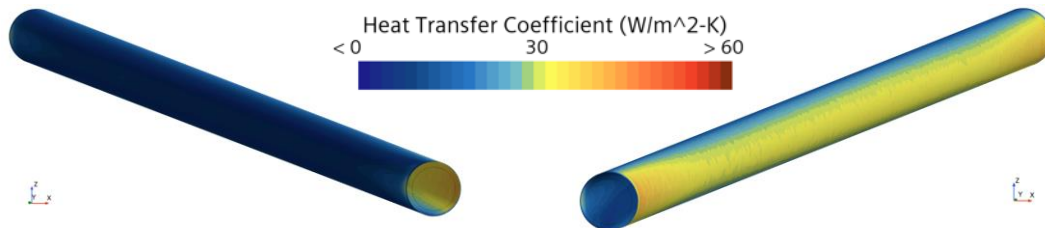


Figure 4.12 a, b) Air velocity contours from case 1 simulation without and with upstream wall, respectively

In Figure 4.12, the right column, the pipe area is shown with difference boundary for contour. According to Figure 4.12b, the wall acts as a barrier in the air flow and reduces air velocity in the wake area where pipe is located. But this wall has also created a recirculation flow in the wake area. The recirculated flow has caused the air flow over the pipe resulting in the remaining heat transfer. To understand the effect of recirculation, heat transfer coefficient on the pipe is compared in Figure 4.13.



(a) Left) upstream side and right) downstream side



(b) Left) upstream side and right) downstream side

Figure 4.13 a, b) Heat transfer coefficient on pipe surface without and with upstream wall

By analyzing the contours from Figure 4.13, we can see that the wall has reduced the HTC in the upstream facing side of the pipe to less than  $5 \text{ W/m}^2 \cdot \text{K}$ . The heat transfer is relatively low in this side that can be said that there is close to no heat transfer. On the downstream facing side after adding the wall, the HTC in the center is not as high as before adding wall but the area with high HTC is expanded more than before adding wall. Since the HTC calculated from simulations is the surface average of the local HTC on the surface, these contours show how the overall HTC is reduced by half. But it can be seen that the effect of recirculation is not as strong to induce an equally high heat transfer on the pipe.

The effect of installing a wall upstream of the coolant pipe on HTC is investigated in this section. According to the results, for multiple simulated cases, the wall has reduced HTC by 50 % in all cases even with higher air flow velocities. It cannot be concluded that this reduction is always the same since it is also dependent on the location and size of the wall. In order to have a general idea of the influence of the wall, further investigation both simulation and experimental should be done in this area.

## 5 Conclusions

In this study, the modeling of heat loss from coolant hoses affected by air flow generated by fan is examined and the results are verified by experimental data obtained in a simplified rig. The focus of this study is on providing a CFD simulation model to predict the heat transfer coefficient of coolant hoses for the purpose of enhancing the accuracy of 1D simulation.

To set up a reliable experiment, a sensitivity analysis is conducted on the measurement devices. According to the analysis, the flowmeter used to measure the coolant flow rate has the most significant influence on accuracy of the results from the experiment. The uncertainty of the results is mostly affected by the uncertainty of the coolant's flowmeter. Hence it is crucial to utilize a flowmeter with relatively high accuracy such as magnetic flowmeter as it is used in this study.

This study aimed to examine the cases with as low coolant flow and as high temperature difference between coolant and air as possible, but the experiment is restricted by the uncertainty of the measurement devices. By reducing the flow rate, the dependency of the uncertainty on the flow rate increases as well as the total uncertainty. As a result, coolant flow rates lower than 0.01 l/s are not examined in the experiment.

In the numerical side of the study, various geometries, mesh settings, boundary conditions, and turbulence models are examined in STARCCM+ to attain the prediction model with highest accuracy. As a result of the studies, steady simulation with turbulence model of k epsilon realizable for both air and coolant side which simulates the whole room of the experiment as well as the fan rotation is chosen to be the best practice of the study. This model is used to predict the heat transfer coefficient in different settings of the rig.

The obtained best-practice for the CFD model is used to forecast the coolant temperature drop and heat transfer coefficient between air and coolant flow. Considering complexity added to the modeling of the room, obtained data from the proposed CFD model match moderately well with the experiment data showing at maximum 15 % error from the range of the uncertainty. The limited accuracy of the measurement devices in the range of the experiment settings, limited further enhancement of the experimental side of the study. It can be concluded either the measurement system is not able to be trusted in the range of the experiment settings or the experimental results are reliable, but the CFD models fail to resolve relevant aspects that could not be detected by the tested variations in boundary conditions and turbulence models. The experiment should be repeated with another measurement devices with higher accuracies to ensure reliable results. If the problem is with CFD side, the error of the simulation results can be corrected on the heat transfer coefficients by an error factor added to the 1 D modeling. Since the focus of this paper is on the heat loss from coolant hoses in the under-hood and the order of magnitude of heat loss is low compared to this study, this approach of correction can be practical.

The final study examined the effect of the placing a wall upstream of the pipe as a barrier to the air flow. The simulated results show a reduction of 50 % in heat transfer coefficient. These results are obtained from a specific configuration of the wall and further investigations needs to be done to get a general conclusion.

Overall, this thesis provided a comprehensive CFD procedure for modeling of heat loss from a coolant pipe affected by the air flow and by doing the sensitivity analysis in experimental side, provided a trustworthy measurement system. This CFD and test model can be utilized for further analysis and different configurations in the subject of heat loss from coolant hoses.

## 6 References

1. Seo, J. H., Patil, M. S., Cho, C. P., & Lee, M. Y. (2018). Heat transfer characteristics of the integrated heating system for cabin and battery of an electric vehicle under cold weather conditions. *International Journal of Heat and Mass Transfer*, 117, 80-94.
2. Zou, H., Wang, W., Zhang, G., Qin, F., Tian, C., & Yan, Y. (2016). Experimental investigation on an integrated thermal management system with heat pipe heat exchanger for electric vehicle. *Energy conversion and management*, 118, 88-95.
3. Zhang, Z., Wang, D., Zhang, C., & Chen, J. (2018). Electric vehicle range extension strategies based on improved AC system in cold climate—A review. *International Journal of Refrigeration*, 88, 141-150.
4. Ma, J., Sun, Y., Zhang, S., Li, J., & Li, S. (2022). Experimental study on the performance of vehicle integrated thermal management system for pure electric vehicles. *Energy Conversion and Management*, 253, 115183.
5. Li, K., Luo, S., Fan, L., Hu, S., Zhou, X., Tu, R., ... & Su, L. (2021). Investigation on the performance and characteristics of a heat pump system for electric vehicles under extreme temperature conditions. *Case Studies in Thermal Engineering*, 27, 101308.
6. Lei, S., Xin, S., & Liu, S. (2022). Separate and integrated thermal management solutions for electric vehicles: A review. *Journal of Power Sources*, 550, 232133.
7. Guo, R., Li, L., Sun, Z., & Xue, X. (2023). An integrated thermal management strategy for cabin and battery heating in range-extended electric vehicles under low-temperature conditions. *Applied Thermal Engineering*, 228, 120502.
8. Rauh, H., März, M., Frey, L., & Sültrop, C. (2014). Energy optimized implementation of climatisation systems in electric vehicles with integrated drive components. *In Conference on the Future of Automotive Technology*.
9. Shim, H. R., & Park, J. M. (2011). A Study of the Transient Analysis Technique on the Under Hood Thermal Damage (No. 2011-28-0126). *SAE Technical Paper*.
10. Ljungskog, E., & Nilsson, U. (2014). CFD for Underhood Modeling. Development of an Efficient Method.
11. Borg, A., & Owen, M. (2019). Experimental and CFD Study of Heat Pickup in Cooling System Hoses.
12. Hatton, A. P., James, D. D., & Swire, H. W. (1970). Combined forced and natural convection with low-speed air flow over horizontal cylinders. *Journal of Fluid Mechanics*, 42(1), 17-31.
13. Incropera, F. P., DeWitt, D. P., Bergman, T. L., & Lavine, A. S. (1996). *Fundamentals of heat and mass transfer* (Vol. 6, p. 116). New York: Wiley.
14. Andersson, B., Andersson, R., Håkansson, L., Mortensen, M., Sudiyo, R., & Van Wachem, B. (2011). *Computational fluid dynamics for engineers*. Cambridge university press.
15. What Is Thermocouple Sensor and How Does It Work. (2023, February 9). Retrieved from <https://dewesoft.com/blog/temperature-measurement-thermocouple-sensors>
16. How To Measure Temperature with RTD Sensors. (2023, August 30). Retrieved from <https://dewesoft.com/blog/measure-temperature-with-rtd-sensors>
17. Theory of Magnetic Flow Meters | Emerson US. (n.d.). Retrieved from <https://www.emerson.com/en-us/automation/measurement-instrumentation/flow-measurement/about-magnetic>
18. Siemens. (2022). Electromagnetic flowmeters SITRANS FM MAG 5000/6000 IP67 Operating Instructions. *cache.industry.siemens.com*. Retrieved from [https://cache.industry.siemens.com/dl/files/683/109810683/att\\_1103281/v1/A5E02338368en\\_MAG\\_5000-6000\\_OI\\_en-US.pdf](https://cache.industry.siemens.com/dl/files/683/109810683/att_1103281/v1/A5E02338368en_MAG_5000-6000_OI_en-US.pdf)

19. Comprehensive Renewable Energy. (2012). *Elsevier*. Retrieved from [http://books.google.ie/books?id=HlbsmgEACAAJ&dq=Comprehensive+Renewable+Energy&hl=&cd=1&source=gbs\\_api](http://books.google.ie/books?id=HlbsmgEACAAJ&dq=Comprehensive+Renewable+Energy&hl=&cd=1&source=gbs_api)
20. User Guide. (2023). *Simcenter STAR-CCM+*.
21. BIPM, I., IFCC, I., ISO, I., & IUPAP, O. (2008). Evaluation of measurement data—guide to the expression of uncertainty in measurement, JCGM 100: 2008 GUM 1995 with minor corrections. *Joint Committee for Guides in Metrology*, 98.
22. Bell, S. (2001). Measurement good practice guide no. 11 (issue 2). A beginner's guide to uncertainty of measurement. *National Physical Laboratory Teddington, Middlesex, United Kingdom*.



DEPARTMENT OF MECHANICS AND MARITIME SCIENCES  
CHALMERS UNIVERSITY OF TECHNOLOGY  
Gothenburg, Sweden 2024  
[www.chalmers.se](http://www.chalmers.se)



**CHALMERS**  
UNIVERSITY OF TECHNOLOGY